

Limits on surface gravities of *Kepler* planet-candidate host stars from non-detection of solar-like oscillations

T. L. Campante¹

campante@bison.ph.bham.ac.uk

and

W. J. Chaplin¹, M. N. Lund², D. Huber^{3,4}, S. Hekker^{5,6}, R. A. García⁷, E. Corsaro^{8,9},
R. Handberg¹, A. Miglio¹, T. Arentoft², S. Basu¹⁰, T. R. Bedding¹¹, J. Christensen-Dalsgaard²,
G. R. Davies¹, Y. P. Elsworth¹, R. L. Gilliland¹², C. Karoff², S. D. Kawaler¹³, H. Kjeldsen²,
M. Lundkvist², T. S. Metcalfe^{14,2}, V. Silva Aguirre², D. Stello¹¹

ABSTRACT

We present a novel method for estimating lower-limit surface gravities ($\log g$) of *Kepler* targets whose data do not allow the detection of solar-like oscillations. The method is tested using an ensemble of solar-type stars observed in the context of the *Kepler* Asteroseismic Science Consortium. We then proceed to estimate lower-limit $\log g$ for a cohort of *Kepler* solar-type planet-candidate host stars with no detected

¹School of Physics and Astronomy, University of Birmingham, Edgbaston, Birmingham, B15 2TT, UK

²Stellar Astrophysics Centre (SAC), Department of Physics and Astronomy, Aarhus University, Ny Munkegade 120, DK-8000 Aarhus C, Denmark

³NASA Ames Research Center, MS 244-30, Moffett Field, CA, 94035, USA

⁴NASA Postdoctoral Program Fellow

⁵Astronomical Institute, “Anton Pannekoek”, University of Amsterdam, The Netherlands

⁶Max Planck Institute for Solar System Research, Katlenburg-Lindau, Germany

⁷Laboratoire AIM, CEA/DSM-CNRS-Université Paris Diderot; IRFU/SAP, Centre de Saclay, 91191 Gif-sur-Yvette Cedex, France

⁸Instituut voor Sterrenkunde, KU Leuven, Celestijnenlaan 200D, B-3001 Leuven, Belgium

⁹INAF — Astrophysical Observatory of Catania, Via S. Sofia 78, I-95123 Catania, Italy

¹⁰Department and Astronomy, Yale University, New Haven, CT, 06520, USA

¹¹Sydney Institute for Astronomy, School of Physics, University of Sydney, Sydney, Australia

¹²Center for Exoplanets and Habitable Worlds, The Pennsylvania State University, University Park, PA, 16802, USA

¹³Department of Physics and Astronomy, Iowa State University, Ames, IA, 50011, USA

¹⁴Space Science Institute, Boulder, CO, 80301, USA

oscillations. Limits on fundamental stellar properties, as provided by this work, are likely to be useful in the characterization of the corresponding candidate planetary systems. Furthermore, an important byproduct of the current work is the confirmation that amplitudes of solar-like oscillations are suppressed in stars with increased levels of surface magnetic activity.

Subject headings: methods: statistical — planetary systems — stars: late-type — stars: oscillations — techniques: photometric

1. Introduction

The NASA *Kepler* mission was designed to use the transit method to detect Earth-like planets in and near the habitable zones of late-type main-sequence stars (Borucki et al. 2010; Koch et al. 2010). *Kepler* has yielded several thousands of new exoplanet candidates (Borucki et al. 2011a,b; Batalha et al. 2013b), bringing us closer to one of the mission’s objectives, namely, the determination of planet occurrence rate as a function of planet radius and orbital period. However, indirect detection techniques, such as transit and radial velocity observations, are only capable of providing planetary properties relative to the properties of the host star. Therefore, accurate knowledge of the fundamental properties of host stars is needed to make robust inference on the properties of their planetary companions.

Unfortunately, the vast majority of the planet-candidate host stars – also designated as *Kepler* Objects of Interest or KOIs – are too faint to have measured trigonometric parallaxes, so that most of the currently available stellar parameters rely on a combination of ground-based multi-color photometry, spectroscopy, stellar model atmospheres and evolutionary tracks. This is the case for the *Kepler* Input Catalog (KIC; Brown et al. 2011). Based on an asteroseismic analysis, Verner et al. (2011b) have detected an average overestimation bias of 0.23 dex in the KIC determination of the surface gravity for stars with $\log g_{\text{KIC}} > 4.0$ dex, thus implying an underestimation bias of up to 50% in the KIC radii for stars with $R_{\text{KIC}} < 2 R_{\odot}$ (see also Bruntt et al. 2012). Brown et al. (2011) had flagged this behavior, warning that the KIC classifications tend to give $\log g$ too large for subgiants. This is a natural cause for concern if these values are to be used in the characterization of exoplanetary systems. This situation can be improved for stellar hosts for which high-resolution spectroscopy is available, an example being the metallicity study undertaken by Buchhave et al. (2012) on a sample of F, G and K dwarfs hosting small exoplanet candidates. However, spectroscopic methods are known to suffer from degeneracies between the effective temperature T_{eff} , the iron abundance [Fe/H] and $\log g$, yielding constraints on the stellar mass and radius that are model-dependent (e.g., Torres et al. 2012). The planet-candidate catalog provided by Batalha et al. (2013b), based on the analysis of the first 16 months of data (from quarter Q1 to quarter Q6), includes a valuable revision of stellar properties based on matching available constraints (from spectroscopic solutions, whenever available, otherwise from the KIC) to Yonsei-Yale

evolutionary tracks (Demarque et al. 2004).

Asteroseismology can play an important role in the determination of accurate fundamental properties of host stars. Solar-like oscillations in a few tens of main-sequence stars and subgiants have been detected using ground-based high-precision spectroscopy (e.g., Bouchy & Carrier 2001; Bazot et al. 2011) and ultra-high-precision, wide-field photometry from the *CoRoT* space telescope (e.g., Appourchaux et al. 2008; Michel et al. 2008). *Kepler* photometry has ever since revolutionized the field of solar-like oscillations by leading to an increase of one order of magnitude in the number of such stars with confirmed oscillations (Verner et al. 2011a). In particular, *Kepler* short-cadence data ($\Delta t \sim 1$ min; Gilliland et al. 2010a) make it possible to investigate solar-like oscillations in main-sequence stars and subgiants, whose dominant periods are of the order of several minutes. The information contained in solar-like oscillations allows fundamental stellar properties (i.e., density, surface gravity, mass and radius) to be determined (e.g., Chaplin & Miglio 2013, and references therein). The very first seismic studies of exoplanet-host stars were conducted using ground-based (Bouchy et al. 2005; Vauclair et al. 2008) and *CoRoT* data (Gaulme et al. 2010; Ballot et al. 2011b). Christensen-Dalsgaard et al. (2010) reported the first application of asteroseismology to known exoplanet-host stars in the *Kepler* field. Subsequently, asteroseismology has been used to constrain the properties of *Kepler* host stars in a series of planet discoveries (Batalha et al. 2011; Barclay et al. 2012; Borucki et al. 2012; Carter et al. 2012; Howell et al. 2012; Barclay et al. 2013; Chaplin et al. 2013; Gilliland et al. 2013; Huber et al. 2013b; Van Eylen et al. 2013). Recently, the first systematic study of *Kepler* planet-candidate host stars using asteroseismology was presented by Huber et al. (2013a).

In this work, we present a novel method for placing limits on the seismic and thus fundamental properties of *Kepler* targets whose data do not allow to detect solar-like oscillations (Sect. 2). Our method relies on being able to predict, for a data set of given stellar and instrumental noise, the threshold oscillation amplitude required to make a marginal detection of the oscillations. This threshold amplitude is frequency-dependent, as we shall explain in detail below. Moreover, on the basis of *Kepler* observations we determine the dependence of the maximum mode amplitude of solar-like oscillations on the frequency at which it is attained. As we shall see, this gives a well-defined amplitude trend. By comparing this trend to the frequency-dependent amplitude for marginal detection of the oscillations, we may set limits on the seismic parameters and hence stellar properties that are required for marginal detection. In Sect. 3.1, the method is tested using an ensemble of solar-type stars observed in the context of the *Kepler* Asteroseismic Science Consortium (KASC; Gilliland et al. 2010b; Kjeldsen et al. 2010). Finally, lower-limit $\log g$ estimates are provided for a cohort of *Kepler* solar-type planet-candidate host stars with no detected oscillations (Sect. 3.2). We discuss the potential use and the limitations of our work in Sect. 4.

2. Method description

2.1. Overview

Solar-like oscillations are predominantly global standing acoustic waves. These are p modes (the pressure variation playing the role of the restoring force) and are characterized by being intrinsically damped while simultaneously stochastically excited by near-surface convection (e.g., Christensen-Dalsgaard 2004). Therefore, all stars cool enough to harbor an outer convective envelope may be expected to exhibit solar-like oscillations. In the remainder of this work, the term *solar-type star* will be used to designate a wide range of F, G and K dwarfs and subgiants.

The frequency-power spectrum of the oscillations in solar-type stars and red giants presents a pattern of peaks with near-regular frequency separations (Vandakurov 1967; Tassoul 1980). The most prominent separation is the so-called large frequency separation, $\Delta\nu$, between neighboring overtones having the same spherical angular degree, l . Oscillation mode power is modulated by an envelope that is generally Gaussian-like in shape (e.g., Kallinger et al. 2010). The frequency of the peak of the power envelope of the oscillations, where the observed modes present their strongest amplitudes, is commonly referred to as the frequency of maximum amplitude, ν_{\max} . The maximum height (power spectral density), H_{\max} , of the envelope, and thus the maximum mode amplitude, A_{\max} , are strong functions of ν_{\max} (e.g., Mosser et al. 2012).

Figure 1 shows some examples of idealized limit frequency-power spectra for stars displaying solar-like oscillations. The left-hand panel shows idealized oscillation power envelopes with ν_{\max} ranging from 1000 to 4000 μHz . As ν_{\max} decreases, the heights, H_{\max} , at the center of the power envelopes increase, and the envelopes also get narrower in frequency, with the FWHM being approximately given by $\nu_{\max}/2$ (e.g., Stello et al. 2007; Mosser et al. 2010), implying that most of the mode power is constrained to a range $\pm\nu_{\max}/2$ around ν_{\max} . The right-hand panel shows the result of adding the expected limit background power-spectral density from granulation and instrumental/shot noise. The latter contribution, seen as a constant offset at high frequencies, depends on the stellar magnitude and has been computed following the empirical minimal term model for the noise given in Gilliland et al. (2010a), where one has assumed observations at *Kepler*-band magnitude $m_{\text{Kep}} = 9$. As ν_{\max} decreases, the power from granulation, modeled as a Lorentzian function centered on zero frequency (e.g., Harvey 1985), is seen to increase while becoming more concentrated at lower frequencies (Mathur et al. 2011; Samadi et al. 2013).

Given the noise background and the length of the observations, one may estimate the oscillation amplitudes that are required to make a marginal detection against that background. To that end, we use the method described in Chaplin et al. (2011c). Since the backgrounds presented by stars vary with frequency, the detection test must be applied at different frequencies within a comprehensive frequency range. At each frequency we estimate the signal-to-noise ratio, and hence the mode envelope height and maximum amplitude, needed to detect a spectrum of solar-like oscillations centered on that frequency (see Appendix A for details).

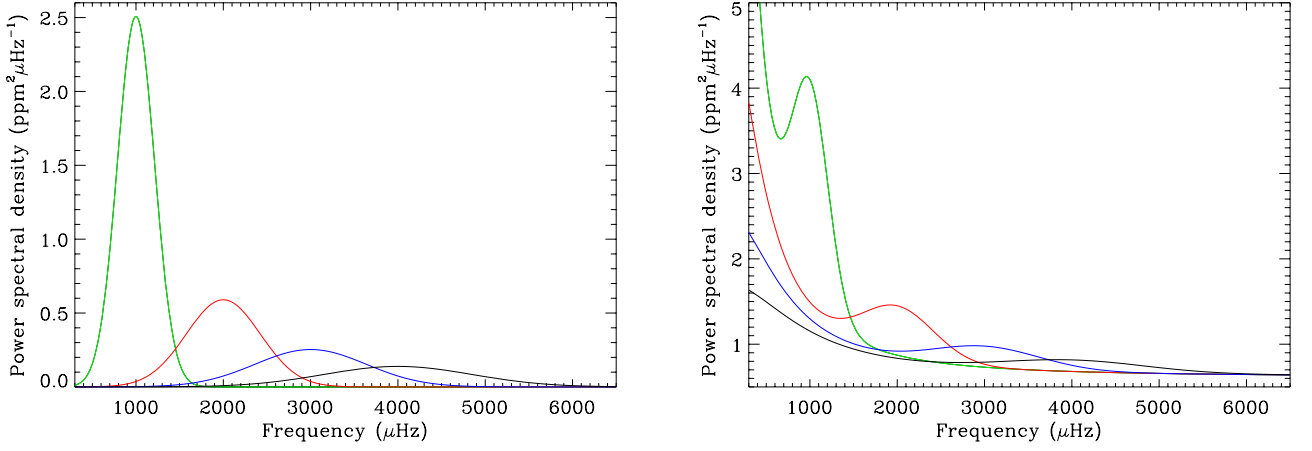


Fig. 1.— Left-hand panel: Idealized oscillation power envelopes for stars showing solar-like oscillations with (from left to right) $\nu_{\max} = 1000, 2000, 3000$ and $4000 \mu\text{Hz}$. Right-hand panel: Resulting idealized limit frequency-power spectra, from combination of oscillation power envelopes and expected background power-spectral densities from granulation and instrumental/shot noise.

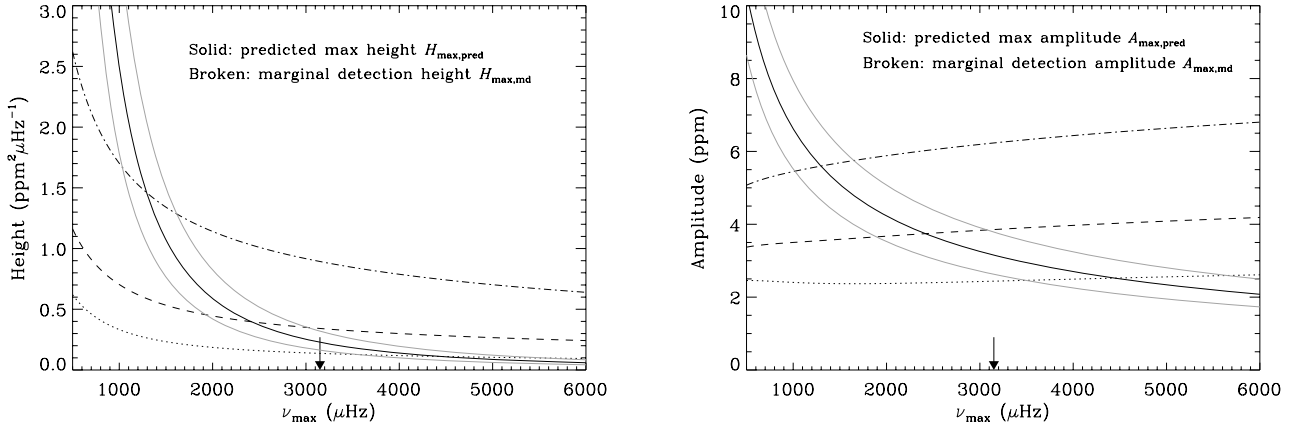


Fig. 2.— Left-hand panel: Predicted trend in the mode power envelope height, $H_{\max,\text{pred}}$, as a function of ν_{\max} (solid black line). Solid gray lines represent the $\pm 1\sigma$ confidence interval on $H_{\max,\text{pred}}$. The frequency-dependent marginal height for detection, $H_{\max,\text{md}}$, is also shown assuming 1-month-long observations of a hypothetical solar twin made at *Kepler*-band magnitudes $m_{\text{Kep}} = 10$ (dotted), $m_{\text{Kep}} = 11$ (dashed) and $m_{\text{Kep}} = 12$ (dot-dashed). The arrow indicates $\nu_{\max,\odot}$. Right-hand panel: Same as left-hand panel, but for the amplitudes.

The left-hand panel of Fig. 2 shows the threshold oscillation power envelope heights, $H_{\max,\text{md}}$, required for marginal detection of oscillations in a hypothetical solar twin. The calculations assumed 1-month-long observations at *Kepler*-band magnitudes $m_{\text{Kep}} = 10$ (dotted), $m_{\text{Kep}} = 11$ (dashed) and $m_{\text{Kep}} = 12$ (dot-dashed). As the noise level rises – here, with increasing value of m_{Kep} – so too do the threshold heights needed for detection. These thresholds also increase with decreasing frequency because the rising backgrounds make it potentially harder to detect the oscillations.

The solid black line shows the expected trend in height, $H_{\max,\text{pred}}$, as a function of ν_{\max} (as per the left-hand panel of Fig. 1), the surrounding lines following the $\pm 1\sigma$ envelope given by analysis of *Kepler* data. This will be discussed in more detail in Sect. 2.3. We note that while this trend is a strong function of ν_{\max} , allowance must also be made for some dependence on the effective temperature T_{eff} (cf. Kjeldsen & Bedding 1995, 2011), and on the stellar activity levels (because elevated levels of activity affect detectability of the oscillations; see García et al. 2010; Chaplin et al. 2011b). Here, we assumed solar values of temperature and activity to get the plotted solid-line trend. A recent account of alternative observational scaling relations aimed at predicting oscillation amplitudes is given in Corsaro et al. (2013). The frequency at which each $H_{\max,\text{md}}$ curve crosses $H_{\max,\text{pred}}$ corresponds to the seismic frequency $\nu_{\max,\text{md}}$ required for marginal detection of solar-like oscillations, given the observed noise background. The uncertainty in $\nu_{\max,\text{md}}$ is then defined by the intersection of $H_{\max,\text{md}}$ with the $\pm 1\sigma$ envelope associated with $H_{\max,\text{pred}}$. From Fig. 2, we see that $\nu_{\max,\text{md}}$ decreases with increasing m_{Kep} as a result of the rising noise level.

The strength of the oscillations at the peak of the envelope is more commonly expressed as an equivalent amplitude, A_{\max} , for radial (i.e., $l=0$) modes rather than as a height, H_{\max} . We may convert the heights to amplitudes using (Kjeldsen et al. 2008; Ballot et al. 2011a):

$$A_{\max} = \sqrt{H_{\max} \Delta\nu / \xi}, \quad (1)$$

where ξ corresponds to the total mode power per $\Delta\nu$ in units of $l=0$ power (viz., it measures the effective number of modes per order). The right-hand panel of Fig. 2 plots threshold amplitudes for detection, $A_{\max,\text{md}}$, and the expected trend in amplitude, $A_{\max,\text{pred}}$ (same line styles as in the left-hand panel). Unlike the threshold heights, the threshold amplitudes are seen to rise with increasing frequency. This is due to the presence of $\Delta\nu$ in Eq. (1), which increases with increasing ν_{\max} (e.g., Stello et al. 2009), more than offsetting the impact of a background that decreases with increasing frequency.

2.2. Limits on surface gravities from marginal detection $\nu_{\max,\text{md}}$

We may convert the marginal detection $\nu_{\max,\text{md}}$ into an equivalent marginal detection surface gravity, g_{md} , for a given data set. The frequency of maximum amplitude, ν_{\max} , is found to scale to very good approximation with the acoustic cutoff frequency (Brown et al. 1991; Kjeldsen & Bedding 1995; Belkacem et al. 2011), which, assuming an isothermal stellar atmosphere, gives a scaling relation for ν_{\max} in terms of surface gravity g and effective temperature T_{eff} . Solving for g and

normalizing by solar properties and parameters, one has

$$g \simeq g_{\odot} \left(\frac{\nu_{\max}}{\nu_{\max,\odot}} \right) \left(\frac{T_{\text{eff}}}{T_{\text{eff},\odot}} \right)^{1/2}, \quad (2)$$

with $g_{\odot} = 27402 \text{ cm s}^{-2}$, $\nu_{\max,\odot} = 3150 \mu\text{Hz}$ and $T_{\text{eff},\odot} = 5777 \text{ K}$. Hence, with independent knowledge of T_{eff} , and substituting $\nu_{\max,\text{md}}$ for ν_{\max} in Eq. (2), we may estimate an equivalent marginal detection surface gravity, g_{md} . It becomes apparent that the surface gravity g is mainly dependent on ν_{\max} , with the latter often taken as an indicator of the evolutionary state of a star. We should note that this so-called “direct method” of estimating stellar properties may lead to unphysically large uncertainties in the derived quantities since scaling relations are not constrained by the equations governing stellar structure and evolution. Alternatively, by comparing theoretical seismic quantities with the observed ones over a large grid of stellar models, very precise determinations of $\log g$ (< 0.05 dex) can be obtained for F, G and K dwarfs (e.g., Creevey et al. 2013).

The accuracy of Eq. (2) has been the subject of several studies. For instance, Huber et al. (2012) found no systematic deviations as a function of evolutionary state when testing the ν_{\max} scaling relation for a small sample of stars with available interferometric data. Based on a comparison involving about forty well-studied late-type pulsating stars with gravities derived using classical methods, Morel & Miglio (2012) found overall agreement with mean differences not exceeding 0.05 dex. Creevey et al. (2013) studied sources of systematic errors in the determination of $\log g$ using grid-based methods and found possible biases of the order of 0.04 dex. Since we are interested in computing an equivalent marginal detection value rather than the value itself, the quoted accuracies will not undermine the purpose of our study. We will adopt a conservative figure of 0.04 dex for the accuracy and adding it in quadrature to the uncertainties produced by Eq. (2).

We may, of course, estimate $\nu_{\max,\text{md}}$ for a *Kepler* data set irrespective of whether or not we have detected oscillations. For a star with data showing detected oscillations it must be the case that the observed maximum amplitude will be greater than or equal to the marginal amplitude for detection (allowing for uncertainty in the measurement), i.e., $A_{\max} \geq A_{\max,\text{md}}$. It must then also be the case that $\nu_{\max} \leq \nu_{\max,\text{md}}$. Inspection of Fig. 2 tells us that this is the case for 1-month-long observations of a solar twin made at $m_{\text{Kep}} = 10$, where we have assumed the solar value of ν_{\max} , i.e., $\nu_{\max,\odot}$. Therefore, we now have an upper-limit estimate of a seismic property of the star. By using Eq. (2), we can translate this into an upper-limit estimate of a fundamental stellar property, to be specific, the surface gravity. In this case the direct determination of ν_{\max} from the observed oscillation power provides an estimate of g . However, in marginal cases the present analysis may serve as a consistency check of the reality of the detected oscillations.

Things get unquestionably more interesting when we consider data on stars for which we have failed to make a detection. Here, it must then be the case that $A_{\max,\text{pred}} < A_{\max,\text{md}}$ or, equivalently, $\nu_{\max} > \nu_{\max,\text{md}}$, meaning that the marginal detection $\nu_{\max,\text{md}}$ gives a lower-limit for the actual ν_{\max} . Again, inspection of Fig. 2 suggests that we would fail to detect oscillations in solar twins with $m_{\text{Kep}} = 11$ and $m_{\text{Kep}} = 12$. Finally, use of Eq. (2) allows us to translate this lower-limit estimate of

ν_{\max} into a lower-limit estimate of the surface gravity.

2.3. Calibration of mode amplitude prediction $A_{\max,\text{pred}}$

To establish a calibration for $A_{\max,\text{pred}}$, we used results on solar-type stars that have been observed in short cadence for at least three consecutive months from Q5 onwards as part of the KASC. We call this cohort 1. Stars in cohort 1 have moderate-to-high S/N in the p modes, which was one of the prerequisites for their selection for long-term observations by *Kepler*. The presence of solar-like oscillations in these stars had previously been confirmed based on observations made during the mission’s survey phase (e.g., Chaplin et al. 2011a). Light curves for these stars were prepared in the manner described by García et al. (2011) and were then high-pass filtered – using a 1-day-cutoff triangular filter – to remove any low-frequency power due to stellar activity and instrumental variability. We also analysed a smaller cohort of *Kepler* solar-type planet-candidate host stars with detected oscillations (cf. Huber et al. 2013a). We call this cohort 2, noting that cohorts 1 and 2 do not overlap. Preparation of the light curves for the stars in this second cohort differed from the procedure described above, although with no discernable impact on the homogeneity of the ensuing analysis. These light curves came from *Kepler* short-cadence data up to Q11. Specifically, transits needed to be corrected, since the sharp features in the time domain would cause significant power leakage from low frequencies into the oscillation spectrum in the frequency domain. This was achieved using a median filter with a length chosen according to the measured duration of the transit.

We extracted the global asteroseismic parameters A_{\max} and ν_{\max} for the stars in both cohorts using the SYD (Huber et al. 2009), AAU (Campante et al. 2010) and OCT (Hekker et al. 2010) automated pipelines. Note that these pipelines were part of a thorough comparison exercise of complementary analysis methods used to extract global asteroseismic parameters of solar-type stars (Verner et al. 2011a). As a preliminary step to the calibration process per se, a validation of the extracted global asteroseismic parameters was carried out based on the prescription of Verner et al. (2011a), which involved the rejection of outliers and a correction to the formal uncertainties returned by each of the analysis methods. The use of three pipelines in the validation of the extracted parameters was deemed sufficient, given the high S/N of the calibration stars. Firstly, we required that for each parameter determined for each star in either cohort, the results from at least two pipelines were contained within a range of fixed relative size centered on the median value (to be specific, $\pm 21.5\%$ for A_{\max} and $\pm 10.5\%$ for ν_{\max}). Results outside this range were iteratively removed until either all results were in agreement or fewer than two results remained. For each analysis method, only those stars with validated results for both parameters were retained. In addition, we demanded that the measured $\nu_{\max} > 350 \mu\text{Hz}$, which approximately corresponds to the base of the red-giant branch (e.g., Huber et al. 2011). Secondly, parameter uncertainties were recalculated by adding in quadrature the formal uncertainty and the standard deviation of the validated results over the contributing pipelines. The final (relative) median uncertainties in A_{\max}

and ν_{\max} for the three analysis methods are seen to lie within 6.9–8.0 % and 2.4–3.1 %, respectively.

We used a Bayesian approach to calibrate a scaling relation for $A_{\max,\text{pred}}$ (for more details, see Corsaro et al. 2013). Two competing scaling relations (or models) were tested. Model \mathcal{M}_1 is based solely on the independent observables ν_{\max} and T_{eff} :

$$\frac{A_{\max,\text{pred}}}{A_{\max,\odot}} \Big|_{\mathcal{M}_1} = \beta \left(\frac{\nu_{\max}}{\nu_{\max,\odot}} \right)^{-s} \left(\frac{T_{\text{eff}}}{T_{\text{eff},\odot}} \right)^{3.5s-r}, \quad (3)$$

where the solar maximum mode amplitude for the *Kepler* bandpass takes the value $A_{\max,\odot} = 2.5\text{ppm}$. The presence of the factor β means that the model needs not to pass through the solar point. Model \mathcal{M}_1 has the same functional form as model $\mathcal{M}_{1,\beta}$ of Corsaro et al. (2013). The effective temperatures used here and in the remainder of this work were derived by Pinsonneault et al. (2012), who performed a recalibration of the KIC photometry in the Sloan Digital Sky Survey (SDSS) *griz* filters using YREC models. Model \mathcal{M}_2 , on the other hand, includes an extra exponential relation in the magnetic activity proxy, ζ_{act} :

$$\frac{A_{\max,\text{pred}}}{A_{\max,\odot}} \Big|_{\mathcal{M}_2} = \beta \left(\frac{\nu_{\max}}{\nu_{\max,\odot}} \right)^{-s} \left(\frac{T_{\text{eff}}}{T_{\text{eff},\odot}} \right)^{3.5s-r} e^{m \zeta_{\text{act}}}. \quad (4)$$

The magnetic activity proxy is described in Appendix B. Four free parameters at most enter the Bayesian inference problem. We have adopted uniform priors for the model parameters s , r , and m , and a Jeffreys’ prior for β , which results in an uniform prior for $\ln \beta$. Table 1 lists the prior ranges adopted for each model parameter. Furthermore, we do not consider error-free independent variables, which means their relative uncertainties are properly taken into account by the likelihood function.

To proceed with the calibration of a scaling relation for $A_{\max,\text{pred}}$, we now look for an individual set of global asteroseismic parameters A_{\max} and ν_{\max} (i.e., tracing back to a single analysis method), as opposed to some sort of average set, meaning that the parameters used in the calibration are fully reproducible. Furthermore, the fact that the extracted global asteroseismic parameters have been validated gives us confidence to use the output of any of the analysis methods in the calibration process. We opted for using the results arising from the SYD pipeline. The reasons behind this choice are simple: this pipeline generated the largest number of validated stars (163, of which 133 belong to cohort 1) and the broadest coverage in terms of the independent observables in Eqs. (3) and (4): $350 \lesssim \nu_{\max} \lesssim 4400 \mu\text{Hz}$, $4950 \lesssim T_{\text{eff}} \lesssim 7200 \text{K}$ and $10 \lesssim \zeta_{\text{act}} \lesssim 1000 \text{ppm}$. This sample is dominated by main-sequence stars and so no attempt was made to derive separate scaling relations for $A_{\max,\text{pred}}$ based on the evolutionary state of the stars. In fact, for the ranges in ν_{\max} and T_{eff} being considered, the observed logarithmic amplitudes are seen to vary approximately linearly with the logarithmic values of both ν_{\max} and T_{eff} – as reproduced by models \mathcal{M}_1 and \mathcal{M}_2 – with no abrupt change in slope, meaning that evolutionary influences are negligible (see also Corsaro et al. 2013).

Tables 2 and 3 summarize the outcome of the Bayesian estimation of the model parameters. Note that the mean bias is much smaller than the observed scatter (i.e., $\bar{x}_{\text{res}} \ll \sigma_{\text{res}}^w$). Figures 3

and 4 display the predicted and observed amplitudes, as well as the resulting relative residuals, for models \mathcal{M}_1 and \mathcal{M}_2 , respectively. We note that the observed amplitudes of stars in cohort 2 are systematically higher than those in cohort 1. This is particularly noticeable at $\nu_{\max} \sim 1500 \mu\text{Hz}$ in the top panels of Figs. 3 and 4. Stars in cohort 2 (having a magnitude distribution that peaks at $m_{\text{Kep}} \simeq 12$) are known to be globally fainter than members of cohort 1 (for which the magnitude distribution peaks at $m_{\text{Kep}} \simeq 11$), meaning that the high-frequency noise in the power spectrum will be greater. This leads to a selection bias in the measured amplitudes, viz., being fainter only those stars with the highest amplitudes will have detectable oscillations. In fact, cohort 2 consists primarily of slightly evolved F- and G-type stars (Huber et al. 2013a), which have larger oscillation amplitudes than their unevolved counterparts.

Finally, we computed the so-called Bayes’ factor in order to perform a formal statistical comparison of the two competing models. Computing the Bayes’ factor in favor of model \mathcal{M}_2 over model \mathcal{M}_1 (i.e., $B_{21} \equiv \mathcal{E}_{\mathcal{M}_2} / \mathcal{E}_{\mathcal{M}_1}$, the ratio of the Bayesian evidences) gave a logarithmic factor of $\ln B_{21} \gg 1$, decisively favoring model \mathcal{M}_2 over model \mathcal{M}_1 (Jeffreys 1961). Note that we are not saying that model \mathcal{M}_2 is physically more meaningful, but rather statistically more likely. This in turn renders statistical significance to the inclusion of an extra dependence on ζ_{act} in model \mathcal{M}_2 . The negative value of model parameter m implies that amplitudes of solar-like oscillations are suppressed in stars with increased levels of surface magnetic activity. This corroborates the conclusions of Chaplin et al. (2011b) – where an exponential relation was also considered – and strengthens the quantitative results on stellar activity and amplitudes presented by Huber et al. (2011). Henceforth, we use the calibration for $A_{\text{max,pred}}$ based on model \mathcal{M}_2 (Eq. 4).

Table 1: Prior ranges adopted in the Bayesian estimation of the model parameters.

Parameter	Prior range
$\ln \beta$	$[-0.5, 0.5]$
s	$[0.5, 1.0]$
r	$[2.4, 4.4]$
m	$[-0.2, 0.2]$

Table 2: Expected values of the inferred model parameters and their associated 68.3% Bayesian credible regions. The logarithm of the Bayesian evidence, $\ln \mathcal{E}$, the mean relative residuals, \bar{x}_{res} , and the weighted RMS of the relative residuals, σ_{res}^w , are also reported.

Model	$\ln \beta$	s	r	m	$\ln \mathcal{E}$	\bar{x}_{res}	σ_{res}^w
				$(\times 10^{-4} \text{ ppm}^{-1})$			
\mathcal{M}_1	$0.09^{+0.01}_{-0.02}$	$0.71^{+0.01}_{-0.01}$	$3.42^{+0.11}_{-0.10}$...	-469.8	-0.015 ± 0.001	0.17
\mathcal{M}_2	$0.22^{+0.02}_{-0.02}$	$0.68^{+0.02}_{-0.02}$	$2.83^{+0.14}_{-0.13}$	$-9.5^{+0.9}_{-0.8}$	-24.3	-0.038 ± 0.001	0.14

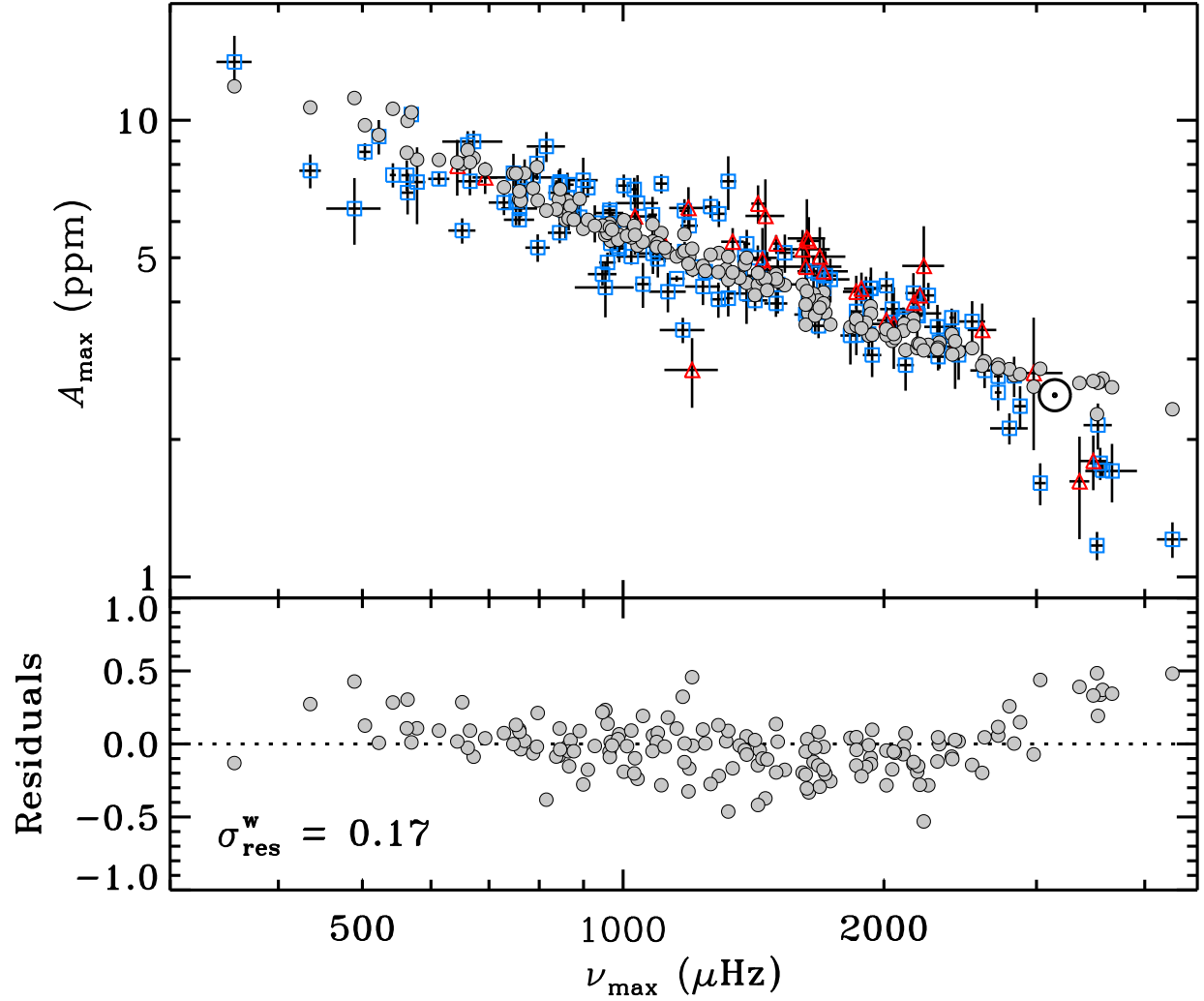


Fig. 3.— Calibration of the amplitude scaling relation (or model) \mathcal{M}_1 . Top panel: Predicted amplitudes (filled gray circles) are plotted against the measured ν_{\max} . Observed amplitudes are shown in the background for stars both in cohort 1 (open blue squares) and cohort 2 (open red triangles). The solar symbol is placed according to the adopted solar reference values. Bottom panel: Relative residuals in the sense (Predicted – Observed)/Predicted. Also shown is the weighted RMS of the relative residuals, an indicator of the quality of the fit.

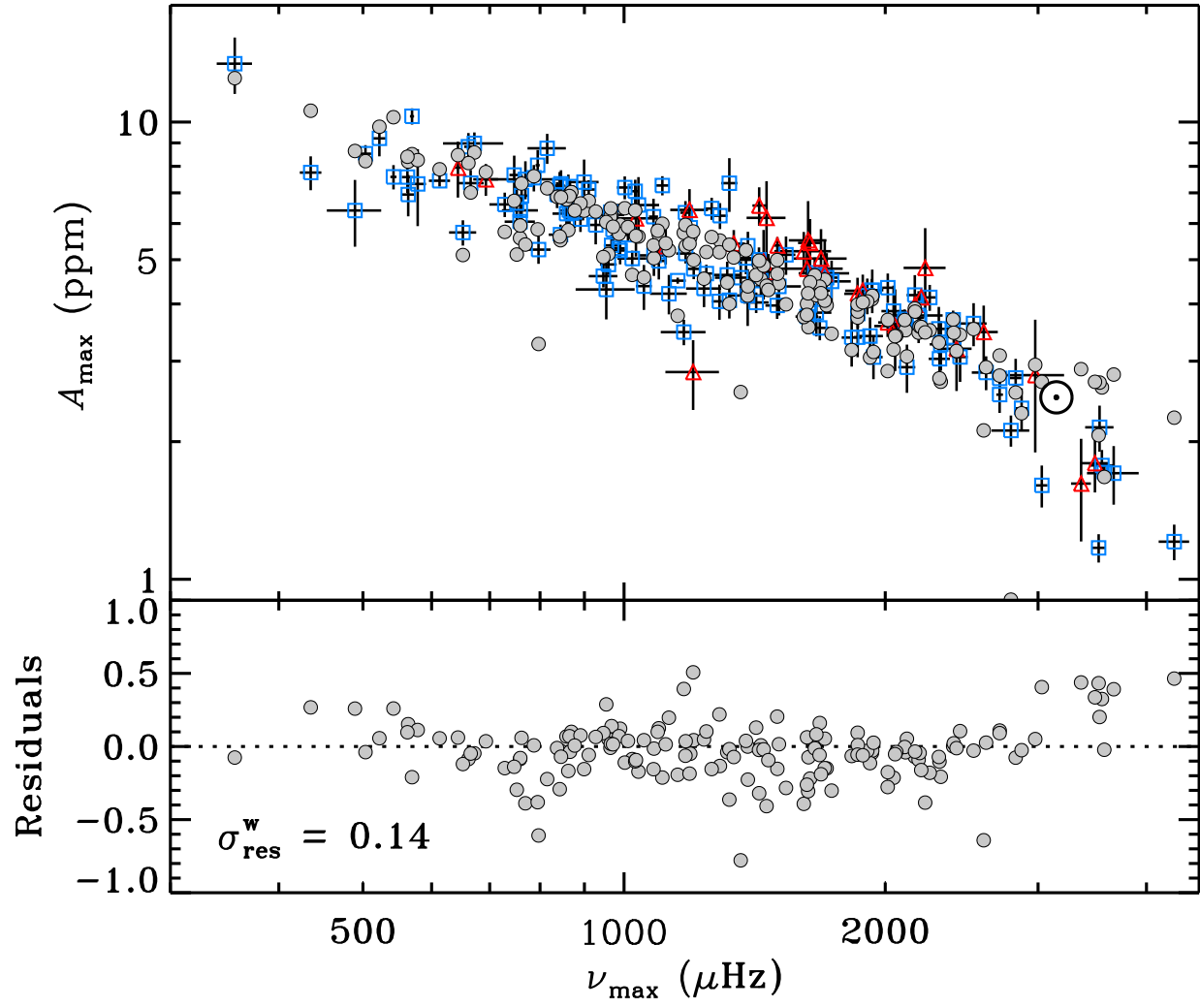


Fig. 4.— Same as Fig. 3, but for scaling relation (or model) \mathcal{M}_2 .

Table 3: Correlation coefficients for each pair of model parameters.

Model	s vs. r	s vs. $\ln \beta$	s vs. m	r vs. $\ln \beta$	r vs. m	$\ln \beta$ vs. m
\mathcal{M}_1	0.16	-0.81	...	0.31
\mathcal{M}_2	0.40	-0.75	0.01	0.03	0.15	-0.39

3. Results

We have applied the method described above to three non-overlapping cohorts of stars, namely, to solar-type stars with detected oscillations that were observed as part of the KASC (cohort 1, as before), and to solar-type planet-candidate host stars both with (cohort 2, as before) and without (cohort 3) detected oscillations. For every data set in each of these three cohorts, we computed the mode amplitude threshold $A_{\max, \text{md}}$ as a function of frequency (cf. Appendix A). We compared this to the mode amplitude prediction $A_{\max, \text{pred}}$ for that star (computed using the known T_{eff} and a proxy measure of its activity; cf. Sect. 2.3), which yielded the sought-for $\nu_{\max, \text{md}}$ (cf. Sect. 2.1) and g_{md} (cf. Sect. 2.2).

3.1. Solar-type stars with detected oscillations

As a sanity check on the marginal detection methodology, we began by analyzing solar-type stars for which the presence of oscillations had previously been confirmed. The top panel of Fig. 5 shows the computed $\nu_{\max, \text{md}}$ versus the observed ν_{\max} for stars in cohort 1. We depict only stars with validated values of ν_{\max} coming from the SYD pipeline. Since these stars have detections, our sanity check amounts to verifying that $\nu_{\max} \leq \nu_{\max, \text{md}}$, which is indeed found to be the case (with all points lying well above the one-to-one line). Notice that, as a general rule, the brighter the star the higher is $\nu_{\max, \text{md}}$ (and the farther it lies above the one-to-one line), thus making it possible to detect oscillations with even the highest ν_{\max} . The bottom panel of Fig. 5 plots the corresponding marginal detection surface gravities, g_{md} , versus the seismically determined gravities from Chaplin et al. (2014). It must be the case for these stars that $g \leq g_{\text{md}}$ (cf. Eq. 2). Again, the sanity check is seen to hold well.

A similar check was done that focused on stars belonging to cohort 2 (see Fig. 6). The observed ν_{\max} values in the top panel are taken from Huber et al. (2013a) and limited to $\nu_{\max} > 350 \mu\text{Hz}$. Note that for some of the stars, the estimation of ν_{\max} was deemed unreliable by those authors due to the low signal-to-noise ratio in the oscillation spectrum (represented by open symbols). Not all of the depicted stars have actually entered the calibration (as is the case in Fig. 5), and we have thus been careful to guarantee that they comply with the considered ranges in T_{eff} and ζ_{act} . The reference (seismically determined) surface gravities in the bottom panel of Fig. 6 also come from Huber et al. (2013a). Once more, the sanity check is seen to hold, while resulting in less conservative estimates of $\nu_{\max, \text{md}}$ and g_{md} , that is to say, they lie closer to the one-to-one line. We

attribute this mainly to the fact that stars in cohort 2 are globally fainter than stars in cohort 1 (as already mentioned in Sect. 2.3). The sole apparent outlier in the bottom panel of Fig. 6 (in the sense of not being consistent with the one-to-one relation at the 1σ level) corresponds to KOI-168 ($m_{\text{Kep}}=13.44$), which has an unreliable estimation of ν_{max} .

3.2. Solar-type stars without detected oscillations

We now turn our attention to the analysis of *Kepler* solar-type planet-candidate host stars with no detected oscillations (cohort 3), with the intention of providing lower-limit $\log g$ estimates. The light curves for these targets come from available *Kepler* short-cadence data up to Q14. Preparation of these light curves has been done in the same way as for targets in cohort 2 (cf. Sect. 2.3). Selected targets comply with the ranges in T_{eff} and ζ_{act} adopted in the calibration process. This gives a total of 453 targets.

We compared the marginal detection surface gravities, g_{md} , with the spectroscopic values from Buchhave et al. (2012) for stars common to both sets (see Fig. 7). Of the 69 common stars, 16 are saturated (viz., the underlying $\nu_{\text{max,md}}$ equals the lower boundary of the tested frequency range, set at $350 \mu\text{Hz}$) and have not been plotted. This leaves 53 useful data points. Of these, 49 (50 if we allow for the uncertainty in $\log g$ alone) fall below the one-to-one line. This general trend is to be expected for stars with no detected oscillations, for which $g > g_{\text{md}}$. A potential application of our method could be to identify those KOIs that were misclassified as subgiants by Buchhave et al. (2012). Taking $\log g = 3.85$ dex as an indicative cutoff between main-sequence stars and subgiants, we point out that KOI-4 ($\log g = 3.68 \pm 0.10$ dex, $\log g_{\text{md}} = 4.06_{-0.09}^{+0.08}$ dex) has possibly been misclassified as a subgiant. We should note that this cutoff is dependent on stellar mass and metallicity, as well as on the amount of overshooting when a convective core is present. Specifying this cutoff at $\log g = 3.85$ dex serves merely to illustrate this potential application of the method.

Comparison with the $\log g$ values from Batalha et al. (2013b) for stars common to both sets is shown in Fig. 8. These values do not come with an associated error bar and so we have adopted the standard deviations of the residuals in table 4 of Huber et al. (2013a) as notional error bars. Accordingly, for $\log g < 3.85$ ($\log g > 3.85$): $\sigma_{\log g} = 0.11$ (0.12) for stars with spectroscopic follow-up, otherwise $\sigma_{\log g} = 0.50$ (0.29) for stars with available KIC parameters only¹. Of the 354 stars common to both sets, 190 are saturated. This leaves 164 useful data points. Of these, 94% of the points (98% if we allow for the uncertainty in $\log g$ alone) fall below the one-to-one line. Three KOIs have possibly been misclassified as subgiants by Batalha et al. (2013b): KOI-4 ($\log g = 3.81 \pm 0.11$ dex, $\log g_{\text{md}} = 4.06_{-0.09}^{+0.08}$ dex), KOI-100 ($\log g = 3.69 \pm 0.11$ dex, $\log g_{\text{md}} = 4.12_{-0.10}^{+0.11}$ dex) and KOI-1001 ($\log g = 3.80 \pm 0.50$ dex, $\log g_{\text{md}} = 3.92_{-0.08}^{+0.07}$ dex). Notice that KOI-4 has once again been listed as a misclassified subgiant.

¹Note that an uncertainty of 0.4 dex is typically assumed in the KIC for $\log g$ (e.g., Verner et al. 2011b).

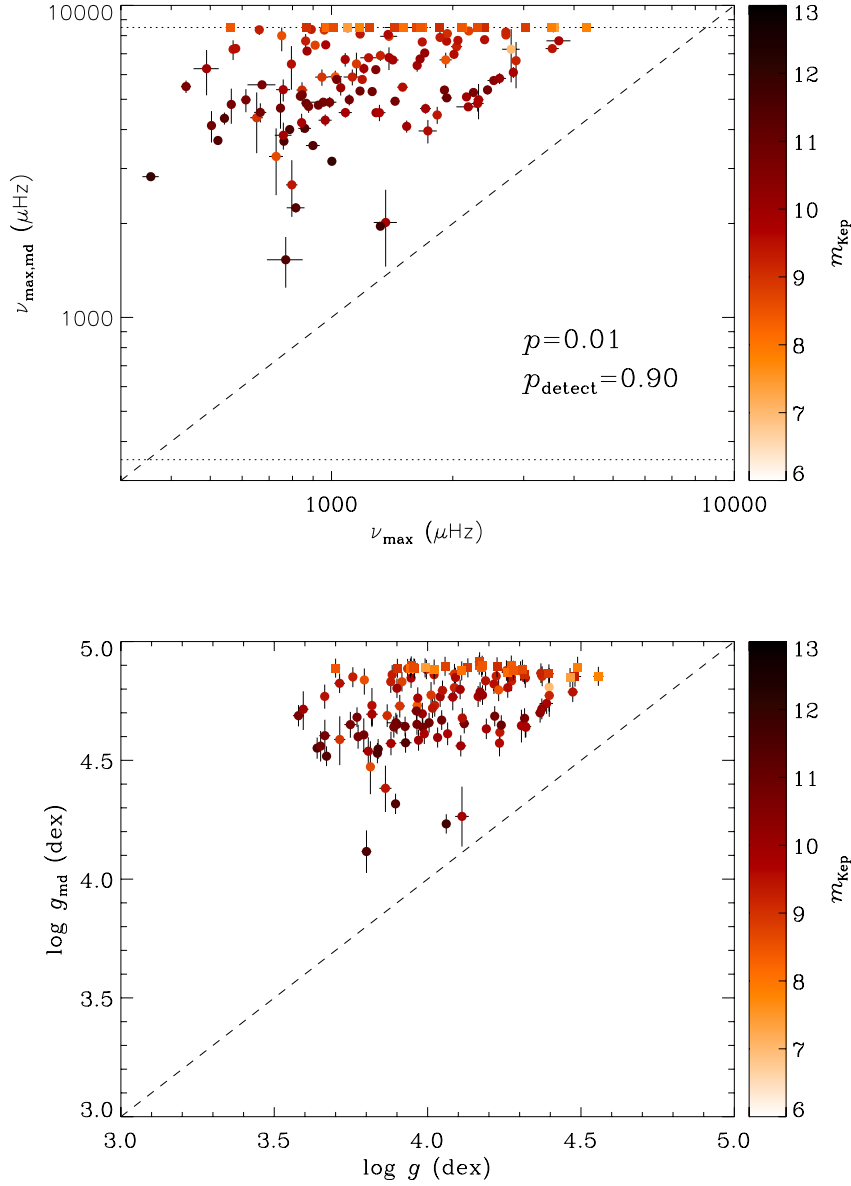


Fig. 5.— Top panel: Computed $\nu_{\max,md}$ versus the measured ν_{\max} (from the SYD pipeline) for solar-type stars showing oscillations observed as part of the KASC (cohort 1). Horizontal dotted lines delimit the range in frequency that has been tested in the determination of $\nu_{\max,md}$ (to be specific, from $350\mu\text{Hz}$ to the Nyquist frequency for *Kepler* short-cadence data, $\nu_{\text{Nyq}} \sim 8496\mu\text{Hz}$). The adopted p -value and detection probability are indicated. Bottom panel: Corresponding marginal detection gravities, g_{md} , versus the seismically determined gravities from Chaplin et al. (2014). In both panels, the dashed line represents the one-to-one relation. Filled squares indicate that the determination of $\nu_{\max,md}$ has saturated (viz., $\nu_{\max,md}$ equals the upper boundary of the tested frequency range). Points are colored according to magnitude.

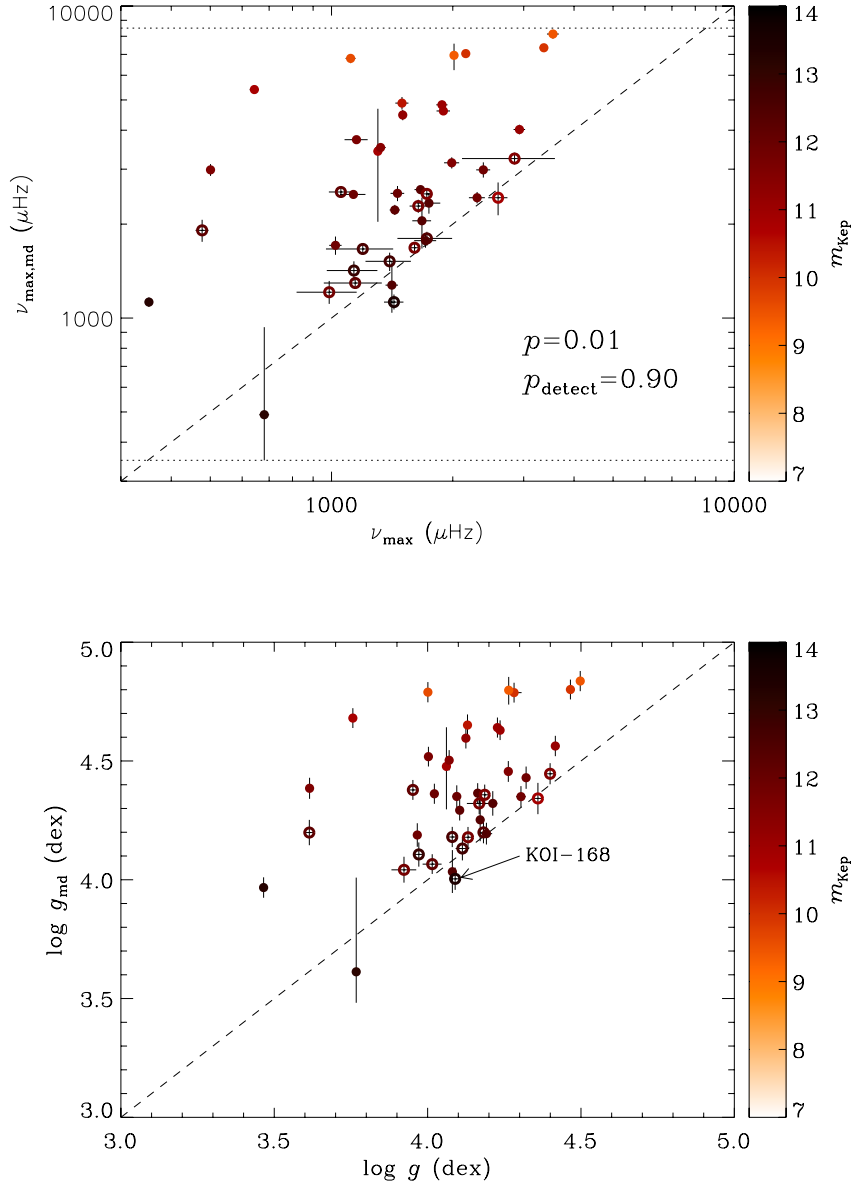


Fig. 6.— Top panel: Computed $\nu_{\max,\text{md}}$ versus the measured ν_{\max} (from Huber et al. 2013a) for solar-type planet-candidate host stars showing oscillations (cohort 2). Horizontal dotted lines delimit the range in frequency that has been tested in the determination of $\nu_{\max,\text{md}}$ (to be specific, from 350 μHz to the Nyquist frequency, ν_{Nyq}). The adopted p -value and detection probability are indicated. Bottom panel: Corresponding marginal detection gravities, g_{md} , versus the seismically determined gravities from Huber et al. (2013a). In both panels, the dashed line represents the one-to-one relation. Points are colored according to magnitude. Stars for which the estimation of ν_{\max} was deemed unreliable by those authors are represented by open symbols.

We propose lower-limit $\log g$ estimates for *Kepler* solar-type planet-candidate host stars with no detected oscillations, as given in Table 4. We have discarded targets for which the determination of $\nu_{\max, \text{md}}$ has saturated, since the associated marginal detection surface gravities are not bona fide lower-limit $\log g$ estimates. This leaves 220 targets of the potential 453 targets mentioned above. The faintest target in this subset of 220 stars has $m_{\text{Kep}} = 14.73$, in contrast with $m_{\text{Kep}} = 16.42$ for the full cohort. Clearly, target saturation is closely linked to faint magnitudes (cf. Fig. 2). The final median uncertainty in $\log g_{\text{md}}$ is 0.06 dex (or 0.04 dex if we do not include the figure of 0.04 dex added in quadrature to the uncertainties produced by Eq. 2).

Inspection of Fig. 8 reveals that, in most cases, the proposed $\log g_{\text{md}}$ are significantly smaller than the $\log g$ values. This is particularly true for the faintest stars, as can be seen around $\log g \sim 4.4$ dex. In order to evaluate the performance of our method, we computed $\Delta \log g$, i.e., the difference between the $\log g$ from Batalha et al. (2013b) and the proposed $\log g_{\text{md}}$ (individual $\Delta \log g$ are given in Table 4; mean $\Delta \log g$ and associated scatter are given in Table 5). We started by categorizing the stars into two uniform intervals in $\log g$. We restricted ourselves to main-sequence stars (i.e., $\log g \gtrsim 3.85$ dex), since these make up the vast majority of the plotted data points. We further distinguished between bright ($m_{\text{Kep}} \leq 12.4$) and faint ($m_{\text{Kep}} > 12.4$) targets, with $m_{\text{Kep}} = 12.4$ being the magnitude of the faintest host star with detected oscillations among those close to the main sequence (Huber et al. 2013a). The mean $\Delta \log g$ are to be compared with the notional uncertainties on $\log g$ quoted above (i.e., $\sigma_{\log g} = 0.12$ for stars with spectroscopic follow-up, otherwise $\sigma_{\log g} = 0.29$ for stars with available KIC parameters only). We first notice an increase in the mean $\Delta \log g$ with $\log g$. This is in part tied to the variation with $\log g$ of the maximum allowed excursion for $\Delta \log g$, imposed by the lower boundary of the tested frequency range (which translates into a $\log g_{\text{md}} \sim 3.5$ dex floor). The effect of the stellar magnitude is conspicuous. The $\Delta \log g$ for bright stars (15% of the plotted data points in Fig. 8) are on average commensurate with or smaller than the magnitude of the quoted uncertainties on $\log g$, rendering the $\log g_{\text{md}}$ estimates useful. On the other hand, the $\Delta \log g$ for faint stars are on average considerably larger than (for $4.30 \leq \log g \leq 4.75$; 62% of the data points) or at most commensurate with (for $3.85 \leq \log g < 4.30$; 21% of the data points) the uncertainties on $\log g$. Stellar magnitude then strongly affects the usefulness of the $\log g_{\text{md}}$ estimates, especially for faint stars with $\log g \geq 4.30$ in the Batalha et al. (2013b) catalog (e.g., see locus of KOI-201 in Fig. 8). We have not yet mentioned the effect of the length of the observations, which may explain part of the observed scatter. This effect is, nonetheless, considerably weaker than that of the stellar magnitude. This is especially true for the faintest stars, for which multi-year observations are needed to produce a noticeable rise in the detection probability (cf. Chaplin et al. 2011c). In such cases, an upgrade of a few observing months would produce no apparent change in the computed $\log g_{\text{md}}$.

Table 5. Mean differences between $\log g$ values from Batalha et al. (2013b) and proposed $\log g_{\text{md}}$.

	$3.85 \leq \log g < 4.30$		$4.30 \leq \log g \leq 4.75$	
	$m_{\text{Kep}} \leq 12.4$	$m_{\text{Kep}} > 12.4$	$m_{\text{Kep}} \leq 12.4$	$m_{\text{Kep}} > 12.4$
$\Delta \log g$ (dex)	0.01 ± 0.02 (0.12)	0.29 ± 0.01 (0.22)	0.19 ± 0.02 (0.15)	0.658 ± 0.006 (0.25)

Note. — Error bars are given by the standard error of the mean. Numbers in brackets are the standard deviation of the residuals.

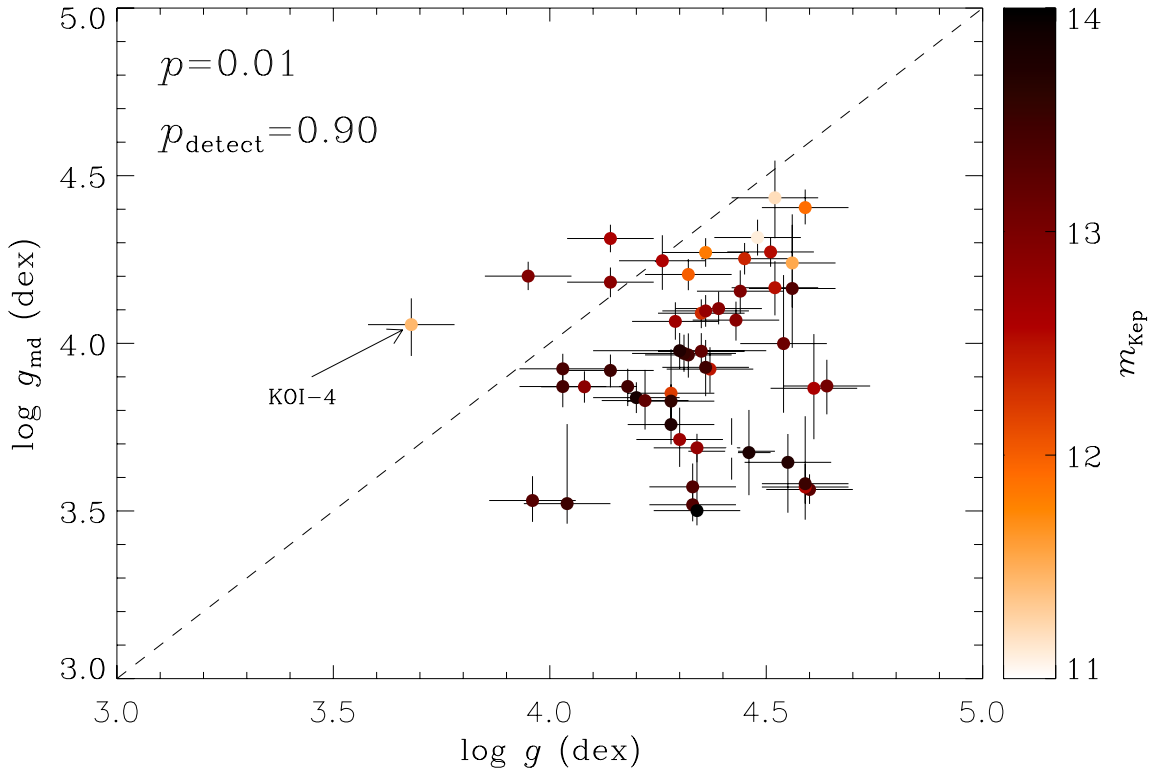


Fig. 7.— Computed marginal detection surface gravities, g_{md} , versus the spectroscopic values from Buchhave et al. (2012) for *Kepler* solar-type planet-candidate host stars with no detected oscillations. The dashed line represents the one-to-one relation. Points are colored according to magnitude. The adopted p -value and detection probability are indicated.

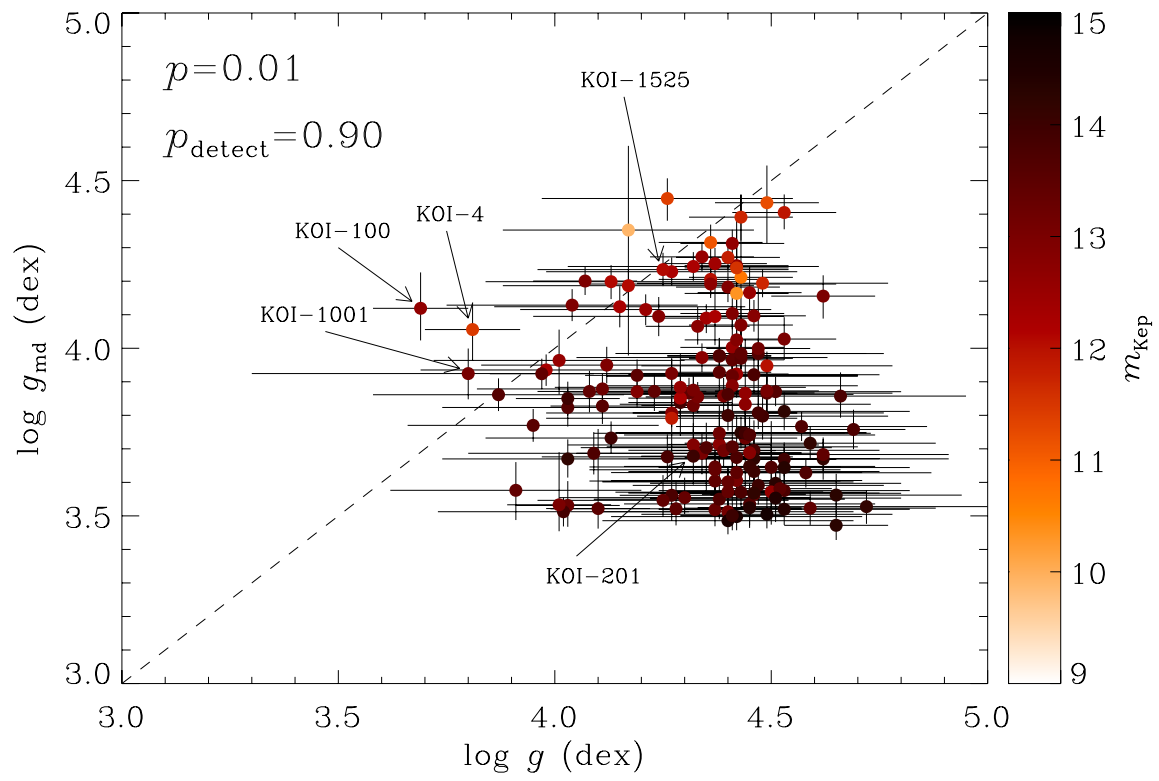


Fig. 8.— Same as Fig. 7, but for the comparison with the $\log g$ values from Batalha et al. (2013b).

4. Summary and discussion

We have presented a novel method for placing limits on the seismic (i.e., ν_{\max}) and hence fundamental properties (i.e., $\log g$) of *Kepler* targets in the data on which we have not been able to detect signatures of solar-like oscillations. For a given noise background and length of the observations, we showed how to estimate the (frequency-dependent) maximum mode amplitude, $A_{\max, \text{md}}$, required to make a marginal detection against that background. We then established a calibration for the predicted maximum mode amplitude, $A_{\max, \text{pred}}$, as a function of ν_{\max} , T_{eff} and ζ_{act} . Comparing $A_{\max, \text{md}}$ to $A_{\max, \text{pred}}$ then yielded $\nu_{\max, \text{md}}$. Finally, use of a scaling relation allowed $\log g_{\text{md}}$ to be computed.

A proxy of the level of stellar activity, ζ_{act} , has been introduced that can be obtained directly from the light curve. This proxy could prove useful in future activity-cycle studies. An important byproduct of the calibration process for $A_{\max, \text{pred}}$ has been the confirmation that amplitudes of solar-like oscillations are suppressed in stars with increased levels of surface magnetic activity.

As a sanity check, the method was first tested on two distinct cohorts of stars showing detected oscillations, namely, on solar-type stars observed as part of the KASC and on solar-type KOIs. For a star with detected oscillations it must be the case that $\nu_{\max} \leq \nu_{\max, \text{md}}$ or, equivalently, $g \leq g_{\text{md}}$. Therefore, the marginal detection g_{md} must be an upper-limit estimate of the actual surface gravity. This sanity check was seen to hold well.

Conversely, for a star for which we failed to make a detection, it must then be the case that $\nu_{\max} > \nu_{\max, \text{md}}$ or, equivalently, $g > g_{\text{md}}$. Therefore, the marginal detection g_{md} must now be a lower-limit estimate of the actual surface gravity. While bearing in mind the existing limitations on the determination of accurate $\log g$ estimates for *Kepler* planet-candidate host stars (cf. Sect. 1), we nonetheless compared our marginal detection $\log g_{\text{md}}$ with the $\log g$ values from Buchhave et al. (2012) and Batalha et al. (2013b), largely confirming our expectations of finding the condition $g > g_{\text{md}}$ to be generally satisfied. We have proposed lower-limit $\log g$ estimates for 220 solar-type KOIs ($m_{\text{Kep}} < 15$) with no detected oscillations. We evaluated the performance of our method based on a comparison of the (mean) deviation, $\Delta \log g$, of the proposed $\log g_{\text{md}}$ from the $\log g$ values in Batalha et al. (2013b), with the quoted uncertainties on $\log g$. As a result, we pointed out the reduced usefulness of $\log g_{\text{md}}$ estimates for faint stars (i.e., $m_{\text{Kep}} > 12.4$) with $\log g \geq 4.30$ in the Batalha et al. (2013b) catalog, which comprise 62% of the plotted data points in Fig. 8. We should, however, note the potential biases affecting stellar properties in that catalog. Huber et al. (2013a) showed surface gravities for subgiant and giant host stars based on high-resolution spectroscopy to be systematically overestimated. Besides, surface gravities for unevolved stars based on KIC parameters were also found to be systematically overestimated in that catalog. A correction for these biases (not applied in this work) would bring the plotted data points in Fig. 8 closer to the one-to-one line, thus improving the perceived performance of our method. Furthermore, we should note that a KIC $\log g > 4$ does not necessarily mean that the possibility of a star being a giant is ruled out (Mann et al. 2012). Consequently, for a typical star with $\log g \sim 4.4$ and $\log g_{\text{md}} \sim 3.5$ (see

Fig. 8), the proposed marginal detection surface gravity may still be a useful constraint by ruling out the giant scenario.

The information contained in the $\log g_{\text{md}}$ estimates is likely to be useful in the characterization of the corresponding candidate planetary systems, namely, by helping constrain possible false-positive scenarios (and thus promote candidates to genuine exoplanets), and/or by constraining the transit model for systems that have already been validated. We give two specific examples that illustrate the potential use of the proposed $\log g_{\text{md}}$ estimates, one being characterized by $\Delta \log g \sim 0$ (KOI-1525) and the other by $\Delta \log g < 0$ (KOI-100):

1. KOI-1525 (see Fig. 8) has no spectroscopic follow-up and a $\log g$ based on the KIC: $\log g = 4.2 \pm 0.4$ dex (where we have assumed a typical KIC uncertainty of 0.4 dex for $\log g$). Hence, this star could either be a subgiant or a main-sequence star, with a radius uncertainty of about 60%. The non-detection of oscillations yields $\log g_{\text{md}} = 4.23_{-0.05}^{+0.05}$ dex, thus ruling out the subgiant scenario. This is likely a main-sequence star of spectral type F ($T_{\text{eff}} = 6905 \pm 87$ K). Evidently, the proposed lower-limit $\log g$ will help to better characterize the two planet candidates detected in this system. The moderate observed level of activity for this relatively bright target ($m_{\text{Kep}} < 12.4$) does not alone explain the absence of detected oscillations². In fact, there is a well-known high-temperature fall-off in the proportion of confirmed solar-like oscillators starting at ~ 6700 K (Verner et al. 2011a), in agreement with the location of the red edge of the classical instability strip. We attribute the absence of detected oscillations mainly to the latter effect.
2. KOI-100 (already highlighted in Sect. 3.2) has spectroscopic follow-up yielding $\log g = 3.69 \pm 0.11$ dex. The non-detection of oscillations yields $\log g_{\text{md}} = 4.12_{-0.10}^{+0.11}$ dex, showing that the spectroscopic classification is erroneous and that the star is less evolved than previously assumed, likely an F-type star ($T_{\text{eff}} = 6743 \pm 140$ K) residing close to the main-sequence. The same reasons invoked above to explain the absence of detected oscillations in KOI-1525 apply here, to which we should add the target’s faintness ($m_{\text{Kep}} > 12.4$). The computed $\log g_{\text{md}}$ then suggests that the currently assumed size of the transiting object based on the spectroscopic solution ($\sim 22 R_{\oplus}$) is too large, and that the companion is likely a genuine planet rather than a low-mass star or brown dwarf. Again, the proposed lower-limit $\log g$ clearly contributes to better characterizing the planet candidate.

This work is an example of the enduring synergy between asteroseismology and exoplanetary science. Throughout the course of the *Kepler* mission, asteroseismology has played an important role in the characterization of planet-candidate host stars. Here, we give continuity to this effort

²We should, however, note that the stellar inclination along the line of sight affects the apparent (i.e., observed) value of the magnetic activity proxy ζ_{act} , if we assume that the stellar variability in solar-type stars is dominated by contributions from active latitudes like for the Sun. Consequently, an intrinsically active star observed at a low angle of inclination may present a moderate-to-low activity proxy.

by providing limits on stellar properties of planet-candidate host stars from the non-detection of solar-like oscillations.

Kepler was competitively selected as the tenth Discovery mission. Funding for this mission is provided by NASA’s Science Mission Directorate. The authors wish to thank the entire *Kepler* team, without whom these results would not be possible. TLC, WJC, RH, AM, GRD and YPE acknowledge the support of the UK Science and Technology Facilities Council (STFC). The research leading to these results has received funding from the European Community’s Seventh Framework Programme (FP7/2007–2013) under grant agreement no. 312844 (SPACEINN). Funding for the Stellar Astrophysics Centre is provided by The Danish National Research Foundation (Grant DNRF106). The research is supported by the ASTERISK project (ASTERoseismic Investigations with SONG and *Kepler*) funded by the European Research Council (Grant agreement no.: 267864). DH is supported by an appointment to the NASA Postdoctoral Program at Ames Research Center, administered by Oak Ridge Associated Universities through a contract with NASA. SH acknowledges financial support from the Netherlands Organization for Scientific Research (NWO). SH acknowledges support from the European Research Council under the European Community’s Seventh Framework Programme (FP7/2007–2013)/ERC grant agreement no. 338251 (StellarAges). EC acknowledges financial support from the European Research Council under the European Community’s Seventh Framework Programme (FP7/2007–2013)/ERC grant agreement no. 227224 (PROSPERITY), from the Fund for Scientific Research of Flanders (G.0728.11), from the Belgian federal science policy office (C90291 Gaia-DPAC), and from Project ASK under grant agreement no. PIRSES-GA-2010-269194. SB acknowledges support from NSF grant AST-1105930 and NASA grant NNX13AE70G. TSM acknowledges NASA grant NNX13AE91G.

A. Computation of mode amplitude threshold $A_{\max, \text{md}}$

Chaplin et al. (2011c) devised a statistical test for predicting the detectability of solar-like oscillations in any given *Kepler* target. The same test is used in this work, although employed in the reverse order. In other words, given the probability of detecting the oscillations, we may translate it into a global measure of the signal-to-noise ratio in the oscillation spectrum, S/N_{tot} , required to make a marginal detection. Finally, knowledge of the noise background will make it possible to compute the mode amplitude threshold, $A_{\max, \text{md}}$, required for detection. The noise background is frequency-dependent, and so too will be $A_{\max, \text{md}}$, meaning that the statistical test must be applied at different frequencies. These frequencies can be regarded as proxies of ν_{\max} . The steps involved in the computation of $A_{\max, \text{md}}$ are summarized next:

1. Computation of S/N_{thresh} :

- (a) A total of N independent frequency bins enter the estimation of S/N_{tot} :

$$N = \nu_{\max, \text{proxy}} T, \tag{A1}$$

where T is the length of the observations. We have assumed that the mode power is contained within a range $\pm\nu_{\max,\text{proxy}}/2$ around $\nu_{\max,\text{proxy}}$.

- (b) We begin by testing the H_0 or null hypothesis (i.e., that we observe pure noise). When binning over N bins, the statistics of the power spectrum of a pure noise signal is taken to be χ^2 with $2N$ degrees of freedom (Appourchaux 2004). By specifying a p -value, we proceed with the numerical computation³ of the detection threshold S/N_{thresh} :

$$p = \int_x^\infty \frac{\exp(-x')}{\Gamma(N)} x'^{(N-1)} dx', \quad (\text{A2})$$

where $x = 1 + S/N_{\text{thresh}}$ and Γ is the gamma function. According to Eqs. (A1) and (A2), an increase in T results in a reduction in S/N_{thresh} . Hence, for a given underlying S/N_{tot} , the oscillation power will be more noticeable against the background as T increases.

2. Computation of S/N_{tot} : The probability, p_{detect} , that S/N_{tot} exceeds S/N_{thresh} is also given by Eq. (A2), although by instead setting $x = (1 + S/N_{\text{thresh}})/(1 + S/N_{\text{tot}})$. This step can be thought of as testing the H_1 or alternative hypothesis (i.e., that we observe a signal embedded in noise). Having adopted a detection probability, p_{detect} , we again have to rely on a numerical computation in order to obtain S/N_{tot} . We adopted $p = 0.01$ and $p_{\text{detect}} = 0.90$ throughout this work.

3. Computation of $A_{\max,\text{md}}$:

- (a) S/N_{tot} is given by the ratio of the total mean mode power, P_{tot} , to the total background power across the frequency range occupied by the oscillations, B_{tot} . The latter is approximately given by

$$B_{\text{tot}} \approx b_{\max} \nu_{\max,\text{proxy}}, \quad (\text{A3})$$

where b_{\max} is the background power-spectral density from granulation and instrumental/shot noise at $\nu_{\max,\text{proxy}}$. For a given data set we determined the background power-spectral density in one of two ways: (i) by fitting a Harvey-like profile plus a constant offset to the power spectrum when oscillations are present (e.g., Karoff et al. 2013, and references therein); or (ii) by applying a median filter when no oscillations are present.

- (b) The total mean mode power, P_{tot} , may be approximately expressed as

$$P_{\text{tot}} \approx 1.55 A_{\max}^2 \eta^2 \frac{\nu_{\max,\text{proxy}}}{\Delta\nu}, \quad (\text{A4})$$

where η takes into account the apodization of the oscillation signal due to the sampling. From Eqs. (A3) and (A4), we obtain

$$A_{\max,\text{md}} = \left(\frac{1}{1.55 \eta^2} \Delta\nu b_{\max} S/N_{\text{tot}} \right)^{1/2}. \quad (\text{A5})$$

³A formula for the percent point function of the χ^2 distribution does not exist in a simple closed form and hence it is computed numerically.

A value of $\Delta\nu$ consistent with $\nu_{\max,\text{proxy}}$ can be obtained from a scaling relation between $\Delta\nu$ and ν_{\max} (e.g., Stello et al. 2009). The computation of $A_{\max,\text{md}}$ incorporates the effect of the observing conditions, namely, the length of the observations via the quantity T (Eq. A1) and the stellar magnitude via the quantity b_{\max} (Eqs. A3 and A5; since the instrumental/shot noise level is magnitude-dependent).

B. Computation of magnetic activity proxy

The magnetic activity proxy, ζ_{act} , is simply an estimate of the intrinsic stellar noise and is intended to measure the level of activity of a star. This variability metric ultimately comprises contributions from rotational spot-modulation, chromospheric activity and stellar magnetic cycles. To compute it, we made use of *Kepler* long-cadence data ($\Delta t \sim 30$ min; Jenkins et al. 2010a), whose sampling cadence is adequate for the purpose of this calculation, since it is far exceeded by the typical timescales of the expected contributing factors. Specifically, the PDC (Presearch Data Conditioning) version of the data was used, since it has been corrected for systematic errors by the Science Operations Center (SOC) pipeline (Jenkins et al. 2010b).

The magnetic activity proxy was computed for all targets classified as solar-type stars in the framework of the KASC. This totaled 2750 targets. It should be stressed, however, that there is no guarantee that this sample is exclusively composed of bona fide solar-type stars. Furthermore, the proxy has been computed for an additional 885 KOIs, corresponding to the complete set of KOIs for which short-cadence data are available. Those KOIs for which the ephemerides of the candidate planet(s) are known (see Batalha et al. 2013a) had their transit signals removed prior to the proxy estimation. This was done by removing segments of the time series equal to 1.5 times the transit duration and centered on the time of mid transit. The long-cadence observations of the selected targets were taken from Q0 through Q14. No restrictions have been imposed in terms of magnitude or number of available quarters.

The proxy estimation was performed as follows:

1. For each target, we applied a binning of 11 data points (~ 5.5 hr) to each quarter of data⁴. The proxy was then given, for each quarter Q_i , by a constant scale factor k times the median absolute deviation⁵ (MAD) of the smoothed time series, i.e., $\zeta_{\text{act},Q_i} = k \cdot \text{MAD}_{Q_i}$. The uncertainty in the quarterly proxy, ζ_{error,Q_i} , was given by $\zeta_{\text{act},Q_i} / \sqrt{2(N_i - 1)}$, where N_i is

⁴A binning of 11 data points translates into an effective cutoff of 0.43d (3-dB bandwidth), meaning that one should get a sensible measure of the magnetic activity level even for the fastest rotators in the sample (with rotational periods $P_{\text{rot}} \gtrsim 0.5$ d).

⁵For a univariate data set, the MAD is defined as the median of the absolute deviations from the data’s median. The multiplicative constant is taken to be $k = 1.4826$, thus converting the MAD into a consistent estimator of the standard deviation, under the assumption of normally distributed data.

the number of data points in Q_i . The reason for using the MAD relies on the fact that it is a robust measure of statistical dispersion, being less prone to outliers than the standard deviation about the mean. The latter has been used by García et al. (2010) to define what they termed the starspot proxy.

2. A magnitude-dependent additive correction was applied to the quarterly proxy estimates to take into account the contribution due to instrumental/shot noise. To implement this correction, we used the minimal term model for the noise proposed by Jenkins et al. (2010a), which gives the RMS noise, $\hat{\sigma}_{\text{lower}}$, per integration. Since the time series were binned over M points ($M = 11$ in the present case), the additive correction to be removed from ζ_{act, Q_i} was just $\hat{\sigma}_{\text{lower}}/\sqrt{M}$.
3. The magnetic activity proxy, ζ_{act} , was taken as the median of the quarterly proxy estimates, with an associated uncertainty (ζ_{error}) given by the MAD of those same quarterly estimates times the constant scale factor k .

Figures 9 and 10 display the results of the proxy estimation in the form of scatter plot matrices for the KASC targets and KOIs, respectively. As desired, no correlation is seen between the magnitude and the value of the proxy. The same holds true between the applied correction and the proxy.

REFERENCES

- Appourchaux, T. 2004, *A&A*, 428, 1039
- Appourchaux, T., Michel, E., Auvergne, M., et al. 2008, *A&A*, 488, 705
- Ballot, J., Barban, C., & van’t Veer-Menneret, C. 2011a, *A&A*, 531, A124
- Ballot, J., Gizon, L., Samadi, R., et al. 2011b, *A&A*, 530, A97
- Barclay, T., Huber, D., Rowe, J. F., et al. 2012, *ApJ*, 761, 53
- Barclay, T., Burke, C. J., Howell, S. B., et al. 2013, *ApJ*, 768, 101
- Batalha, N. M., Borucki, W. J., Bryson, S. T., et al. 2011, *ApJ*, 729, 27
- Batalha, N. M., Rowe, J. F., Bryson, S. T., et al. 2013a, *VizieR Online Data Catalog*, 220, 40024
- . 2013b, *ApJS*, 204, 24
- Bazot, M., Ireland, M. J., Huber, D., et al. 2011, *A&A*, 526, L4
- Belkacem, K., Goupil, M. J., Dupret, M. A., et al. 2011, *A&A*, 530, A142

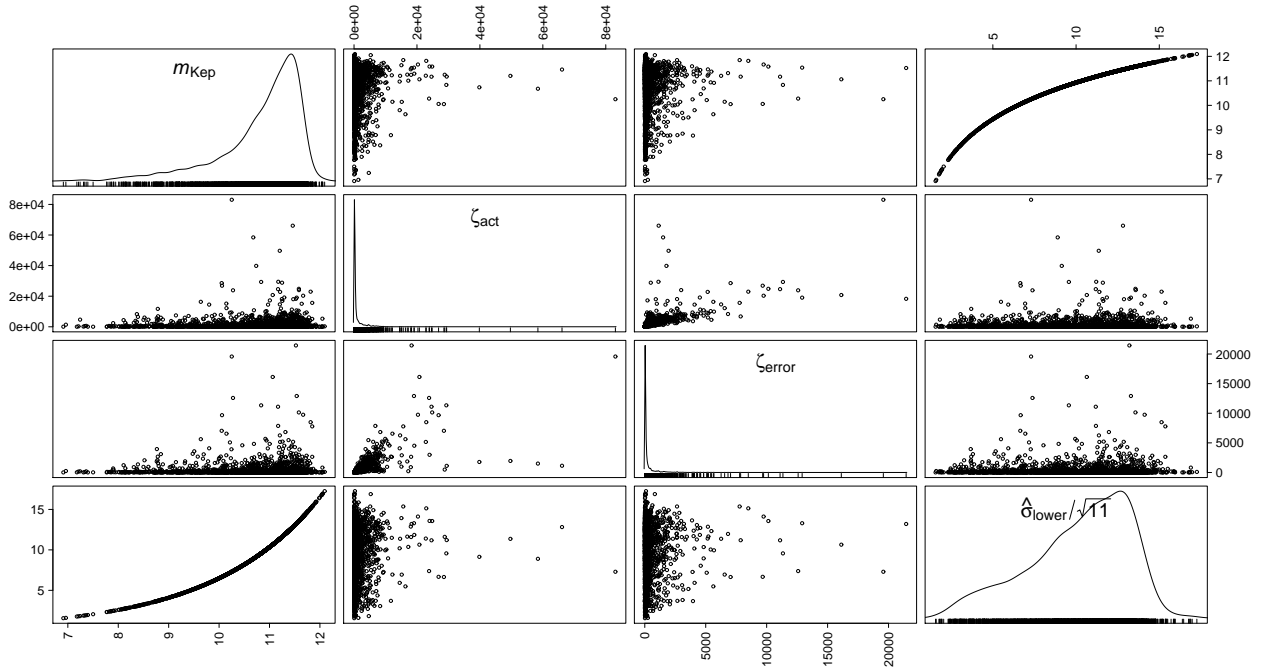


Fig. 9.— Scatter plot matrix showing the results of the proxy estimation for the KASC targets. Parameters entering the plots are the *Kepler*-band magnitude (m_{Kep}), the magnetic activity proxy (ζ_{act}), the uncertainty in the proxy (ζ_{error}) and the applied correction ($\hat{\sigma}_{\text{lower}}/\sqrt{11}$). The curves in the diagonal panels represent the density distributions of the indicated parameters (ticks on the horizontal axis mark the position of each data point). Off-diagonal panels display all the possible pairwise correlations.

- Borucki, W. J., Koch, D., Basri, G., et al. 2010, *Science*, 327, 977
- Borucki, W. J., Koch, D. G., Basri, G., et al. 2011a, *ApJ*, 728, 117
- . 2011b, *ApJ*, 736, 19
- Borucki, W. J., Koch, D. G., Batalha, N., et al. 2012, *ApJ*, 745, 120
- Bouchy, F., Bazot, M., Santos, N. C., Vauclair, S., & Sosnowska, D. 2005, *A&A*, 440, 609
- Bouchy, F., & Carrier, F. 2001, *A&A*, 374, L5
- Brown, T. M., Gilliland, R. L., Noyes, R. W., & Ramsey, L. W. 1991, *ApJ*, 368, 599
- Brown, T. M., Latham, D. W., Everett, M. E., & Esquerdo, G. A. 2011, *AJ*, 142, 112
- Bruntt, H., Basu, S., Smalley, B., et al. 2012, *MNRAS*, 423, 122
- Buchhave, L. A., Latham, D. W., Johansen, A., et al. 2012, *Nature*, 486, 375
- Campante, T. L., Karoff, C., Chaplin, W. J., et al. 2010, *MNRAS*, 408, 542
- Carter, J. A., Agol, E., Chaplin, W. J., et al. 2012, *Science*, 337, 556
- Chaplin, W. J., & Miglio, A. 2013, *ARA&A*, 51, 353
- Chaplin, W. J., Kjeldsen, H., Christensen-Dalsgaard, J., et al. 2011a, *Science*, 332, 213
- Chaplin, W. J., Bedding, T. R., Bonanno, A., et al. 2011b, *ApJ*, 732, L5
- Chaplin, W. J., Kjeldsen, H., Bedding, T. R., et al. 2011c, *ApJ*, 732, 54
- Chaplin, W. J., Sanchis-Ojeda, R., Campante, T. L., et al. 2013, *ApJ*, 766, 101
- Chaplin, W. J., Basu, S., Huber, D., et al. 2014, *ApJS*, 210, 1
- Christensen-Dalsgaard, J. 2004, *Sol. Phys.*, 220, 137
- Christensen-Dalsgaard, J., Kjeldsen, H., Brown, T. M., et al. 2010, *ApJ*, 713, L164
- Corsaro, E., Fröhlich, H.-E., Bonanno, A., et al. 2013, *MNRAS*, 430, 2313
- Creevey, O. L., Thévenin, F., Basu, S., et al. 2013, *MNRAS*, 431, 2419
- Demarque, P., Woo, J.-H., Kim, Y.-C., & Yi, S. K. 2004, *ApJS*, 155, 667
- García, R. A., Mathur, S., Salabert, D., et al. 2010, *Science*, 329, 1032
- García, R. A., Hekker, S., Stello, D., et al. 2011, *MNRAS*, 414, L6
- Gaulme, P., Deheuvels, S., Weiss, W. W., et al. 2010, *A&A*, 524, A47

- Gilliland, R. L., Jenkins, J. M., Borucki, W. J., et al. 2010a, *ApJ*, 713, L160
- Gilliland, R. L., Brown, T. M., Christensen-Dalsgaard, J., et al. 2010b, *PASP*, 122, 131
- Gilliland, R. L., Marcy, G. W., Rowe, J. F., et al. 2013, *ApJ*, 766, 40
- Harvey, J. 1985, in *ESA Special Publication, Vol. 235, Future Missions in Solar, Heliospheric & Space Plasma Physics*, ed. E. Rolfe & B. Battrock, 199–208
- Hekker, S., Broomhall, A.-M., Chaplin, W. J., et al. 2010, *MNRAS*, 402, 2049
- Howell, S. B., Rowe, J. F., Bryson, S. T., et al. 2012, *ApJ*, 746, 123
- Huber, D., Stello, D., Bedding, T. R., et al. 2009, *Communications in Asteroseismology*, 160, 74
- Huber, D., Bedding, T. R., Stello, D., et al. 2011, *ApJ*, 743, 143
- Huber, D., Ireland, M. J., Bedding, T. R., et al. 2012, *ApJ*, 760, 32
- Huber, D., Chaplin, W. J., Christensen-Dalsgaard, J., et al. 2013a, *ApJ*, 767, 127
- Huber, D., Carter, J. A., Barbieri, M., et al. 2013b, *Science*, 342, 331
- Jeffreys, H. 1961, *Theory of Probability*, 3rd edn. (Oxford, England: Oxford University Press)
- Jenkins, J. M., Caldwell, D. A., Chandrasekaran, H., et al. 2010a, *ApJ*, 713, L120
- . 2010b, *ApJ*, 713, L87
- Kallinger, T., Weiss, W. W., Barban, C., et al. 2010, *A&A*, 509, A77
- Karoff, C., Campante, T. L., Ballot, J., et al. 2013, *ApJ*, 767, 34
- Kjeldsen, H., & Bedding, T. R. 1995, *A&A*, 293, 87
- . 2011, *A&A*, 529, L8
- Kjeldsen, H., Christensen-Dalsgaard, J., Handberg, R., et al. 2010, *Astronomische Nachrichten*, 331, 966
- Kjeldsen, H., Bedding, T. R., Arentoft, T., et al. 2008, *ApJ*, 682, 1370
- Koch, D. G., Borucki, W. J., Basri, G., et al. 2010, *ApJ*, 713, L79
- Mann, A. W., Gaidos, E., Lépine, S., & Hilton, E. J. 2012, *ApJ*, 753, 90
- Mathur, S., Hekker, S., Trampedach, R., et al. 2011, *ApJ*, 741, 119
- Michel, E., Baglin, A., Auvergne, M., et al. 2008, *Science*, 322, 558

- Morel, T., & Miglio, A. 2012, MNRAS, 419, L34
- Mosser, B., Belkacem, K., Goupil, M.-J., et al. 2010, A&A, 517, A22
- Mosser, B., Elsworth, Y., Hekker, S., et al. 2012, A&A, 537, A30
- Pinsonneault, M. H., An, D., Molenda-Żakowicz, J., et al. 2012, ApJS, 199, 30
- Samadi, R., Belkacem, K., Ludwig, H.-G., et al. 2013, A&A, 559, A40
- Stello, D., Chaplin, W. J., Basu, S., Elsworth, Y., & Bedding, T. R. 2009, MNRAS, 400, L80
- Stello, D., Bruntt, H., Kjeldsen, H., et al. 2007, MNRAS, 377, 584
- Tassoul, M. 1980, ApJS, 43, 469
- Torres, G., Fischer, D. A., Sozzetti, A., et al. 2012, ApJ, 757, 161
- Van Eylen, V., Lund, M. N., Silva Aguirre, V., et al. 2013, ArXiv e-prints, arXiv:1312.4938
- Vandakurov, Y. V. 1967, AZh, 44, 786
- Vauclair, S., Laymand, M., Bouchy, F., et al. 2008, A&A, 482, L5
- Verner, G. A., Elsworth, Y., Chaplin, W. J., et al. 2011a, MNRAS, 415, 3539
- Verner, G. A., Chaplin, W. J., Basu, S., et al. 2011b, ApJ, 738, L28

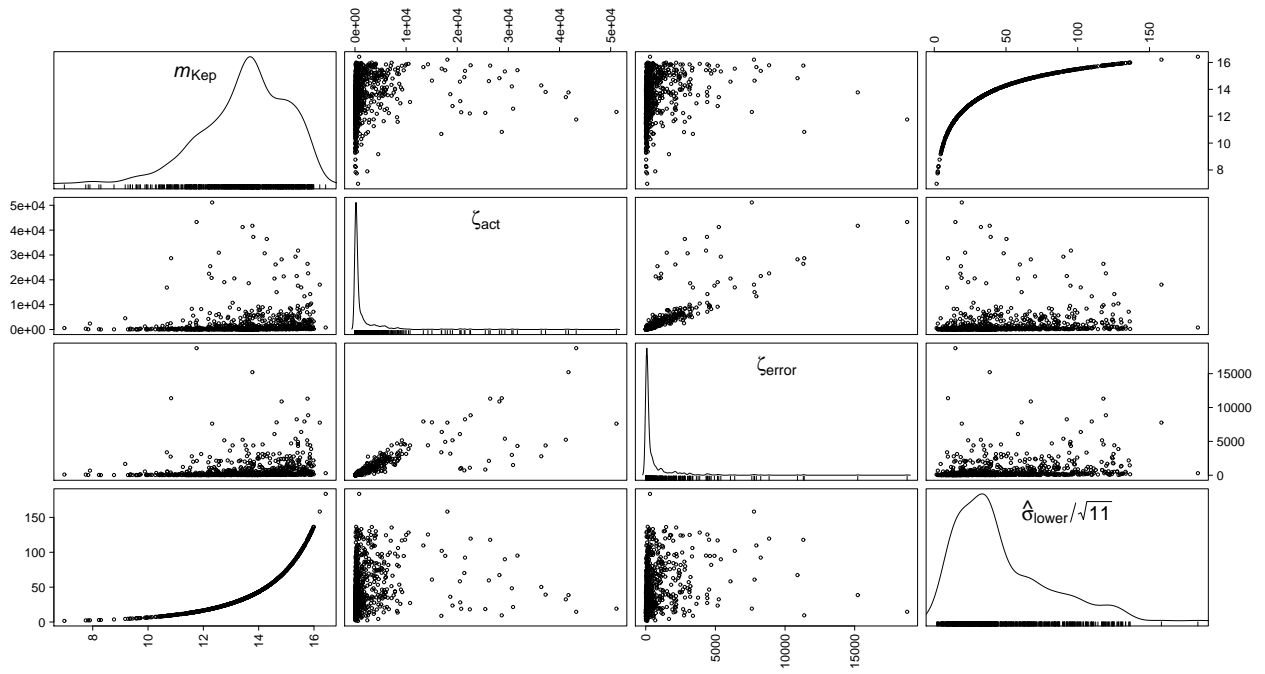


Fig. 10.— Same as Fig. 9, but for the KOIs.

Table 4. Proposed lower-limit $\log g$ estimates for solar-type KOIs with no detected oscillations.

KOI ^a	KIC	m_{Kep}	$T_{\text{eff}}^{\text{b}}$ (K)	ζ_{act} (ppm)	$\log g_{\text{md}}^{\text{c}}$ (dex)	$\Delta \log g$ (dex)
...	10909274	12.153	6594±93	456±376	4.11 ^{+0.22 (0.21)} _{-0.18 (0.17)}	...
...	6131659	12.534	5087±63	797±590	3.78 ^{+0.33 (0.33)} _{-0.23 (0.23)}	...
...	7677005	12.178	6901±94	1011±507	3.88 ^{+0.28 (0.28)} _{-0.25 (0.24)}	...
...	4144236	11.856	6618±101	709±275	4.07 ^{+0.15 (0.15)} _{-0.14 (0.13)}	...
...	6593363	12.893	6170±79	539±293	3.70 ^{+0.17 (0.17)} _{-0.14 (0.13)}	...
...	5653126	13.173	6002±124	641±400	3.68 ^{+0.22 (0.22)} _{-0.16 (0.15)}	...
...	6522750	11.230	5801±59	619±341	4.05 ^{+0.18 (0.18)} _{-0.18 (0.17)}	...
...	2693092	12.003	5996±94	392±263	4.12 ^{+0.15 (0.14)} _{-0.13 (0.13)}	...
4	3861595	11.432	6220±101	583±160	4.06 ^{+0.08 (0.07)} _{-0.09 (0.08)}	-0.25±0.09
6	3248033	12.161	6558±80	195±57	3.95 ^{+0.05 (0.03)} _{-0.05 (0.03)}	...
9	11553706	13.123	6288±72	280±191	3.71 ^{+0.11 (0.10)} _{-0.09 (0.08)}	...
10	6922244	13.563	6392±82	175±51	3.83 ^{+0.05 (0.03)} _{-0.05 (0.04)}	0.28±0.05
11	11913073	13.496	5478±80	371±342	3.58 ^{+0.18 (0.18)} _{-0.10 (0.09)}	...
12	5812701	11.353	6635±71	416±106	4.45 ^{+0.06 (0.04)} _{-0.07 (0.05)}	-0.19±0.06
20	11804465	13.438	6279±89	238±70	3.87 ^{+0.05 (0.03)} _{-0.06 (0.04)}	0.36±0.06
21	10125352	13.396	6414±89	392±95	3.57 ^{+0.07 (0.05)} _{-0.07 (0.05)}	...
22	9631995	13.435	6078±76	209±113	3.97 ^{+0.06 (0.05)} _{-0.07 (0.05)}	0.44±0.07
23	9071386	12.291	6540±81	552±72	3.81 ^{+0.06 (0.05)} _{-0.06 (0.05)}	...
70	6850504	12.498	5540±63	455±137	4.17 ^{+0.08 (0.07)} _{-0.08 (0.07)}	0.28±0.08
78	9764820	10.870	5390±57	244±104	4.32 ^{+0.07 (0.06)} _{-0.06 (0.04)}	...
84	2571238	11.898	5623±57	120±70	4.40 ^{+0.05 (0.04)} _{-0.05 (0.03)}	0.13±0.05
88	7700871	11.871	5801±63	77±44	4.33 ^{+0.05 (0.03)} _{-0.05 (0.02)}	...
91	7747867	11.684	5834±63	192±101	4.14 ^{+0.08 (0.07)} _{-0.07 (0.05)}	...
92	7941200	11.667	6069±69	334±124	4.39 ^{+0.07 (0.05)} _{-0.07 (0.06)}	0.04±0.07
93	6784857	11.477	6279±62	124±11	4.27 ^{+0.04 (0.01)} _{-0.04 (0.01)}	...
99	8505215	12.960	5162±63	230±101	4.16 ^{+0.06 (0.05)} _{-0.07 (0.05)}	0.46±0.06
100	4055765	12.598	6743±140	399±183	4.12 ^{+0.11 (0.10)} _{-0.10 (0.09)}	-0.43±0.10
102	8456679	12.566	6242±138	186±156	4.25 ^{+0.08 (0.06)} _{-0.09 (0.08)}	0.17±0.08
103	2444412	12.593	5766±63	835±280	3.87 ^{+0.16 (0.16)} _{-0.15 (0.15)}	0.57±0.16
105	8711794	12.870	5809±101	75±38	4.18 ^{+0.04 (0.02)} _{-0.04 (0.02)}	0.22±0.04
106	10489525	12.775	6730±133	176±24	3.81 ^{+0.04 (0.01)} _{-0.04 (0.01)}	...
109	4752451	12.385	6201±79	115±35	4.15 ^{+0.04 (0.02)} _{-0.04 (0.02)}	...
110	9450647	12.663	6538±79	52±22	4.19 ^{+0.04 (0.01)} _{-0.04 (0.01)}	0.17±0.04
111	6678383	12.596	6170±65	24±13	4.31 ^{+0.04 (0.01)} _{-0.04 (0.01)}	0.10±0.04
112	10984090	12.772	6125±73	83±57	4.10 ^{+0.05 (0.03)} _{-0.05 (0.03)}	0.36±0.05
114	6721123	12.660	6365±86	140±28	3.86 ^{+0.04 (0.01)} _{-0.04 (0.01)}	...
115	9579641	12.791	6397±91	175±78	4.10 ^{+0.06 (0.04)} _{-0.06 (0.04)}	0.14±0.06
116	8395660	12.882	6280±109	146±52	4.10 ^{+0.05 (0.03)} _{-0.05 (0.03)}	0.31±0.05
120	11869052	12.003	5632±273	188±34	4.05 ^{+0.04 (0.02)} _{-0.05 (0.03)}	...
121	3247396	12.759	6390±85	107±76	3.99 ^{+0.05 (0.03)} _{-0.06 (0.04)}	...
124	11086270	12.935	6314±83	37±30	4.20 ^{+0.04 (0.02)} _{-0.04 (0.01)}	-0.13±0.04
128	11359879	13.758	5841±132	369±208	3.67 ^{+0.13 (0.12)} _{-0.13 (0.12)}	0.75±0.13
129	11974540	13.224	6741±108	328±73	3.76 ^{+0.06 (0.04)} _{-0.05 (0.04)}	...
130	5297298	13.325	6237±105	132±70	3.90 ^{+0.05 (0.04)} _{-0.05 (0.04)}	...
132	8892910	13.794	6176±103	213±34	3.60 ^{+0.05 (0.03)} _{-0.05 (0.03)}	...

Table 4—Continued

KOI ^a	KIC	m_{Kep}	$T_{\text{eff}}^{\text{b}}$ (K)	ζ_{act} (ppm)	$\log g_{\text{md}}^{\text{c}}$ (dex)	$\Delta \log g$ (dex)
134	9032900	13.675	6357±106	226±49	3.79 ^{+0.05 (0.03)} _{-0.05 (0.03)}	...
137	8644288	13.549	5394±91	163±74	3.97 ^{+0.06 (0.04)} _{-0.05 (0.04)}	0.46±0.06
139	8559644	13.492	6145±94	302±152	3.93 ^{+0.08 (0.07)} _{-0.09 (0.08)}	0.45±0.08
141	12105051	13.687	5402±89	481±144	3.65 ^{+0.08 (0.07)} _{-0.15 (0.14)}	0.85±0.12
142	5446285	13.113	5559±79	449±414	4.00 ^{+0.20 (0.20)} _{-0.21 (0.20)}	0.47±0.21
143	4649305	13.682	6984±130	174±47	3.85 ^{+0.05 (0.03)} _{-0.05 (0.03)}	...
146	9048161	13.030	6302±114	151±91	3.92 ^{+0.06 (0.05)} _{-0.07 (0.05)}	...
148	5735762	13.040	5189±71	530±125	3.87 ^{+0.08 (0.07)} _{-0.08 (0.07)}	0.62±0.08
149	3835670	13.397	5718±88	102±39	3.92 ^{+0.04 (0.02)} _{-0.05 (0.02)}	0.05±0.05
150	7626506	13.771	5822±91	160±75	3.92 ^{+0.05 (0.04)} _{-0.06 (0.04)}	0.54±0.05
152	8394721	13.914	6405±103	169±107	3.80 ^{+0.07 (0.05)} _{-0.07 (0.06)}	0.68±0.07
154	9970525	13.174	6510±97	125±43	3.76 ^{+0.05 (0.03)} _{-0.05 (0.03)}	...
155	8030148	13.494	5954±91	75±54	3.92 ^{+0.05 (0.03)} _{-0.05 (0.03)}	0.27±0.05
157	6541920	13.709	5919±95	112±69	3.98 ^{+0.05 (0.03)} _{-0.05 (0.04)}	0.40±0.05
159	8972058	13.431	6069±91	176±34	3.87 ^{+0.05 (0.02)} _{-0.05 (0.02)}	0.44±0.05
160	6631721	13.805	6405±115	119±48	3.77 ^{+0.05 (0.03)} _{-0.05 (0.03)}	...
162	8107380	13.837	5817±95	120±51	3.81 ^{+0.05 (0.02)} _{-0.05 (0.03)}	0.66±0.05
163	6851425	13.536	5264±70	157±64	3.87 ^{+0.05 (0.04)} _{-0.05 (0.03)}	0.62±0.05
165	9527915	13.938	5201±63	293±57	3.67 ^{+0.05 (0.03)} _{-0.05 (0.03)}	0.86±0.05
166	2441495	13.575	5386±83	306±131	3.71 ^{+0.08 (0.07)} _{-0.08 (0.07)}	0.70±0.08
167	11666881	13.273	6485±78	93±44	3.92 ^{+0.05 (0.02)} _{-0.05 (0.03)}	0.49±0.05
169	6185711	13.579	5815±68	240±140	3.61 ^{+0.08 (0.07)} _{-0.09 (0.08)}	...
171	7831264	13.717	6495±105	105±44	3.86 ^{+0.05 (0.02)} _{-0.05 (0.02)}	0.54±0.05
172	8692861	13.749	5886±69	98±93	3.86 ^{+0.07 (0.06)} _{-0.06 (0.05)}	0.80±0.07
173	11402995	13.844	6030±78	72±43	3.84 ^{+0.05 (0.02)} _{-0.05 (0.02)}	0.45±0.05
175	8323753	13.488	6078±95	147±32	3.85 ^{+0.04 (0.02)} _{-0.04 (0.02)}	...
176	6442377	13.432	6568±93	56±39	3.98 ^{+0.04 (0.02)} _{-0.05 (0.02)}	0.45±0.04
177	6803202	13.182	5870±79	93±79	3.98 ^{+0.05 (0.04)} _{-0.06 (0.05)}	0.40±0.06
179	9663113	13.955	6081±90	70±16	3.75 ^{+0.04 (0.01)} _{-0.04 (0.01)}	0.69±0.04
192	7950644	14.221	6195±89	117±89	3.67 ^{+0.06 (0.05)} _{-0.07 (0.05)}	0.79±0.06
198	10666242	14.288	5736±85	108±33	3.63 ^{+0.05 (0.03)} _{-0.06 (0.04)}	...
200	6046540	14.412	5945±119	212±94	3.55 ^{+0.07 (0.06)} _{-0.07 (0.06)}	0.96±0.07
201	6849046	14.014	5629±114	269±158	3.68 ^{+0.10 (0.09)} _{-0.08 (0.07)}	0.64±0.09
209	10723750	14.274	6438±103	217±46	3.75 ^{+0.05 (0.03)} _{-0.05 (0.03)}	0.68±0.05
232	4833421	14.247	6102±84	82±74	3.81 ^{+0.06 (0.04)} _{-0.06 (0.04)}	0.72±0.06
238	7219825	14.061	6274±103	44±18	3.65 ^{+0.04 (0.01)} _{-0.04 (0.01)}	0.80±0.04
241	11288051	14.139	5288±60	119±56	3.53 ^{+0.05 (0.03)} _{-0.05 (0.03)}	1.19±0.05
258	11231334	9.887	6528±91	1242±550	4.35 ^{+0.25 (0.25)} _{-0.37 (0.37)}	-0.18±0.31
259	5790807	9.954	6581±57	362±100	4.50 ^{+0.05 (0.02)} _{-0.06 (0.05)}	...
261	5383248	10.297	5779±66	1209±337	4.16 ^{+0.19 (0.19)} _{-0.18 (0.17)}	0.26±0.18
265	12024120	11.994	6277±62	109±46	4.21 ^{+0.05 (0.02)} _{-0.05 (0.02)}	0.15±0.05
283	5695396	11.525	5875±84	723±268	4.24 ^{+0.14 (0.14)} _{-0.13 (0.13)}	0.18±0.14
284	6021275	11.818	6176±73	57±32	4.27 ^{+0.04 (0.01)} _{-0.04 (0.01)}	0.13±0.04
291	10933561	12.848	5685±63	93±36	3.87 ^{+0.05 (0.02)} _{-0.05 (0.03)}	0.32±0.05
292	11075737	12.872	6025±73	209±90	4.07 ^{+0.06 (0.04)} _{-0.06 (0.05)}	0.36±0.06

Table 4—Continued

KOI ^a	KIC	m_{Kep}	$T_{\text{eff}}^{\text{b}}$ (K)	ζ_{act} (ppm)	$\log g_{\text{md}}^{\text{c}}$ (dex)	$\Delta \log g$ (dex)
294	11259686	12.674	6125±66	244±70	3.83 ^{+0.05 (0.03)} _{-0.05 (0.04)}	0.61±0.05
296	11802615	12.935	6088±68	80±35	3.92 ^{+0.05 (0.02)} _{-0.04 (0.02)}	0.49±0.04
297	11905011	12.182	6282±66	157±28	4.23 ^{+0.04 (0.02)} _{-0.04 (0.01)}	0.04±0.04
301	3642289	12.730	6337±93	58±30	3.97 ^{+0.04 (0.01)} _{-0.04 (0.02)}	0.37±0.04
302	3662838	12.059	6953±103	240±48	4.20 ^{+0.05 (0.03)} _{-0.05 (0.03)}	-0.07±0.05
303	5966322	12.193	5734±60	364±153	4.09 ^{+0.09 (0.08)} _{-0.09 (0.08)}	0.28±0.09
304	6029239	12.549	6150±81	767±177	3.96 ^{+0.09 (0.08)} _{-0.10 (0.09)}	0.05±0.10
307	6289257	12.797	6310±76	188±86	4.02 ^{+0.06 (0.04)} _{-0.06 (0.04)}	0.40±0.06
308	6291837	12.351	6355±83	264±58	4.25 ^{+0.05 (0.02)} _{-0.05 (0.02)}	0.12±0.05
313	7419318	12.990	5331±79	184±96	4.03 ^{+0.06 (0.05)} _{-0.06 (0.05)}	0.50±0.06
316	8008067	12.701	5705±91	244±78	4.07 ^{+0.06 (0.04)} _{-0.05 (0.04)}	0.26±0.06
317	8121310	12.885	6658±126	111±48	4.13 ^{+0.05 (0.03)} _{-0.05 (0.03)}	-0.09±0.05
318	8156120	12.211	6578±78	1133±181	3.85 ^{+0.13 (0.12)} _{-0.11 (0.11)}	0.44±0.12
321	8753657	12.520	5611±57	71±37	4.27 ^{+0.04 (0.02)} _{-0.04 (0.02)}	0.07±0.04
327	9881662	12.996	6354±77	177±64	3.86 ^{+0.05 (0.04)} _{-0.05 (0.03)}	0.53±0.05
328	9895004	12.820	5821±69	746±186	3.73 ^{+0.11 (0.10)} _{-0.12 (0.11)}	...
329	10031885	13.478	6036±75	112±81	3.65 ^{+0.05 (0.03)} _{-0.06 (0.04)}	...
331	10285631	13.497	5555±63	482±379	3.52 ^{+0.24 (0.23)} _{-0.06 (0.04)}	0.58±0.15
332	10290666	13.046	5756±65	68±44	3.86 ^{+0.04 (0.02)} _{-0.05 (0.03)}	0.47±0.05
339	10587105	13.763	6277±73	202±90	3.58 ^{+0.07 (0.05)} _{-0.07 (0.05)}	0.95±0.07
343	10982872	13.203	5945±75	315±153	3.83 ^{+0.09 (0.08)} _{-0.09 (0.08)}	0.49±0.09
344	11015108	13.400	5984±81	301±212	3.65 ^{+0.12 (0.11)} _{-0.12 (0.12)}	0.72±0.12
351	11442793	13.804	6329±86	216±147	3.70 ^{+0.09 (0.08)} _{-0.09 (0.08)}	0.76±0.09
354	11568987	13.235	6282±115	683±186	3.73 ^{+0.11 (0.10)} _{-0.15 (0.14)}	0.71±0.13
365	11623629	11.195	5611±57	221±246	4.43 ^{+0.11 (0.10)} _{-0.12 (0.11)}	0.06±0.12
367	4815520	11.105	5864±60	287±78	4.32 ^{+0.05 (0.04)} _{-0.05 (0.04)}	0.04±0.05
369	7175184	11.992	6377±60	106±33	3.95 ^{+0.04 (0.01)} _{-0.05 (0.02)}	0.54±0.04
373	7364176	12.765	6121±75	110±29	3.69 ^{+0.04 (0.01)} _{-0.04 (0.02)}	0.76±0.04
383	3342463	13.109	6411±88	124±130	3.63 ^{+0.08 (0.06)} _{-0.08 (0.07)}	...
403	4247092	14.169	5784±82	101±54	3.57 ^{+0.05 (0.03)} _{-0.05 (0.04)}	0.89±0.05
405	5003117	14.026	5577±78	194±159	3.57 ^{+0.09 (0.08)} _{-0.09 (0.08)}	...
416	6508221	14.290	5249±72	90±54	3.56 ^{+0.06 (0.05)} _{-0.06 (0.05)}	1.09±0.06
506	5780715	14.731	6021±121	199±103	3.50 ^{+0.08 (0.07)} _{-0.04 (0.01)}	0.99±0.06
508	6266741	14.387	5612±108	202±101	3.52 ^{+0.07 (0.06)} _{-0.06 (0.04)}	0.93±0.06
518	8017703	14.287	5037±63	226±103	3.47 ^{+0.09 (0.08)} _{-0.04 (0.02)}	1.18±0.07
528	9941859	14.598	5674±84	79±47	3.49 ^{+0.06 (0.04)} _{-0.04 (0.01)}	0.91±0.05
567	7445445	14.338	5817±85	202±81	3.64 ^{+0.06 (0.04)} _{-0.07 (0.06)}	0.89±0.07
568	7595157	14.140	5390±81	203±50	3.72 ^{+0.05 (0.03)} _{-0.05 (0.03)}	0.87±0.05
584	9146018	14.129	5524±67	163±89	3.67 ^{+0.06 (0.04)} _{-0.06 (0.05)}	0.95±0.06
591	9886221	14.396	5693±75	59±37	3.56 ^{+0.05 (0.03)} _{-0.05 (0.02)}	...
611	6309763	14.022	6357±102	245±66	3.63 ^{+0.06 (0.04)} _{-0.06 (0.05)}	0.83±0.06
612	6587002	14.157	5231±99	140±76	3.67 ^{+0.06 (0.04)} _{-0.06 (0.04)}	0.36±0.06
625	4449034	13.592	6464±124	278±52	3.86 ^{+0.05 (0.03)} _{-0.05 (0.03)}	0.01±0.05
633	4841374	13.871	6070±113	65±15	3.51 ^{+0.04 (0.01)} _{-0.04 (0.02)}	0.51±0.04
645	5374854	13.716	6306±115	174±95	3.69 ^{+0.06 (0.05)} _{-0.06 (0.05)}	0.40±0.06

Table 4—Continued

KOI ^a	KIC	m_{Kep}	$T_{\text{eff}}^{\text{b}}$ (K)	ζ_{act} (ppm)	$\log g_{\text{md}}^{\text{c}}$ (dex)	$\Delta \log g$ (dex)
649	5613330	13.310	6288±102	101±43	3.55 ^{+0.06 (0.04)} _{-0.05 (0.03)}	0.75±0.05
653	5893123	13.858	6615±136	61±30	3.68 ^{+0.04 (0.02)} _{-0.05 (0.02)}	...
655	5966154	13.004	6463±86	52±34	3.87 ^{+0.04 (0.02)} _{-0.04 (0.02)}	0.45±0.04
659	6125481	13.413	6721±125	135±98	3.55 ^{+0.08 (0.06)} _{-0.05 (0.03)}	0.70±0.06
660	6267535	13.532	5480±74	76±56	3.77 ^{+0.05 (0.03)} _{-0.05 (0.03)}	0.18±0.05
662	6365156	13.336	6148±85	60±35	3.60 ^{+0.04 (0.02)} _{-0.04 (0.02)}	0.80±0.04
664	6442340	13.484	5985±89	148±133	3.52 ^{+0.09 (0.08)} _{-0.05 (0.03)}	0.76±0.07
665	6685609	13.182	6080±87	470±131	3.75 ^{+0.08 (0.07)} _{-0.08 (0.07)}	0.63±0.08
672	7115785	13.998	5760±103	621±215	3.50 ^{+0.19 (0.18)} _{-0.04 (0.02)}	0.91±0.12
680	7529266	13.643	6327±94	140±125	3.70 ^{+0.07 (0.06)} _{-0.13 (0.12)}	0.65±0.10
681	7598128	13.204	6549±96	335±80	3.52 ^{+0.07 (0.06)} _{-0.04 (0.01)}	...
692	8557374	13.648	5806±75	55±26	3.77 ^{+0.04 (0.02)} _{-0.04 (0.02)}	0.80±0.04
693	8738735	13.949	6352±84	187±97	3.57 ^{+0.06 (0.05)} _{-0.07 (0.06)}	0.94±0.07
695	8805348	13.437	6226±80	66±78	3.60 ^{+0.06 (0.05)} _{-0.06 (0.05)}	0.77±0.06
696	8869680	13.357	5966±136	78±33	3.85 ^{+0.04 (0.02)} _{-0.04 (0.01)}	...
700	8962094	13.580	5922±84	42±46	3.98 ^{+0.05 (0.02)} _{-0.05 (0.02)}	0.49±0.05
701	9002278	13.725	5036±66	323±74	3.70 ^{+0.06 (0.04)} _{-0.06 (0.04)}	0.93±0.06
707	9458613	13.988	6212±94	92±58	3.85 ^{+0.05 (0.03)} _{-0.05 (0.03)}	0.18±0.05
708	9530945	13.998	6277±88	147±49	3.59 ^{+0.06 (0.05)} _{-0.06 (0.04)}	0.88±0.06
711	9597345	13.967	5612±103	122±35	3.80 ^{+0.04 (0.02)} _{-0.05 (0.02)}	0.60±0.04
718	9884104	13.764	6029±88	499±143	3.56 ^{+0.13 (0.13)} _{-0.08 (0.06)}	0.71±0.10
968	3560301	10.963	6962±87	151±41	4.19 ^{+0.04 (0.02)} _{-0.04 (0.02)}	...
978	11494130	10.988	6673±107	304±126	4.06 ^{+0.08 (0.07)} _{-0.08 (0.07)}	...
987	7295235	12.550	5482±76	1286±384	3.57 ^{+0.21 (0.21)} _{-0.10 (0.09)}	0.93±0.15
991	10154388	13.581	5938±106	113±70	3.82 ^{+0.06 (0.04)} _{-0.06 (0.04)}	0.21±0.06
1001	1871056	13.038	6235±118	225±123	3.92 ^{+0.07 (0.06)} _{-0.08 (0.07)}	-0.12±0.08
1020	2309719	12.899	6059±85	245±66	3.95 ^{+0.05 (0.04)} _{-0.05 (0.04)}	0.17±0.05
1057	6066416	11.558	6806±93	106±50	4.00 ^{+0.05 (0.03)} _{-0.05 (0.03)}	...
1113	2854914	13.703	6314±115	219±217	3.55 ^{+0.11 (0.11)} _{-0.06 (0.04)}	0.83±0.09
1116	2849805	13.333	6029±94	151±113	3.57 ^{+0.07 (0.06)} _{-0.07 (0.05)}	0.83±0.07
1128	6362874	13.507	5485±63	144±81	3.58 ^{+0.06 (0.04)} _{-0.06 (0.04)}	0.94±0.06
1150	8278371	13.326	5915±73	257±99	3.52 ^{+0.06 (0.05)} _{-0.05 (0.03)}	0.85±0.06
1151	8280511	13.404	5759±70	116±74	3.68 ^{+0.05 (0.03)} _{-0.05 (0.04)}	0.94±0.05
1162	10528068	12.783	6138±82	32±18	3.81 ^{+0.04 (0.01)} _{-0.04 (0.01)}	0.46±0.04
1169	10319385	13.248	5956±77	80±39	3.56 ^{+0.05 (0.02)} _{-0.04 (0.02)}	0.90±0.04
1175	10350571	13.290	5650±65	309±102	3.53 ^{+0.07 (0.06)} _{-0.06 (0.05)}	0.50±0.07
1185	3443790	11.840	6276±63	610±91	3.70 ^{+0.08 (0.07)} _{-0.06 (0.05)}	...
1215	3939150	13.420	6050±94	106±92	3.87 ^{+0.06 (0.05)} _{-0.06 (0.05)}	0.21±0.06
1218	3442055	13.331	5870±85	109±83	3.64 ^{+0.06 (0.04)} _{-0.06 (0.04)}	0.73±0.06
1220	4043190	12.988	5163±68	319±241	3.53 ^{+0.16 (0.15)} _{-0.08 (0.07)}	0.48±0.12
1236	6677841	13.659	6779±103	251±62	3.74 ^{+0.05 (0.04)} _{-0.05 (0.03)}	0.71±0.05
1242	6607447	13.750	6446±120	81±61	3.57 ^{+0.05 (0.03)} _{-0.05 (0.03)}	0.86±0.05
1275	8583696	13.672	5625±77	110±99	3.54 ^{+0.06 (0.05)} _{-0.06 (0.05)}	0.91±0.06
1315	10928043	13.137	6415±88	120±45	3.69 ^{+0.05 (0.04)} _{-0.05 (0.02)}	0.70±0.05
1344	4136466	13.446	6038±70	112±41	3.52 ^{+0.05 (0.03)} _{-0.05 (0.03)}	1.07±0.05

Table 4—Continued

KOI ^a	KIC	m_{Kep}	$T_{\text{eff}}^{\text{b}}$ (K)	ζ_{act} (ppm)	$\log g_{\text{md}}^{\text{c}}$ (dex)	$\Delta \log g$ (dex)
1379	7211221	13.687	5870±70	51±29	3.63 ^{+0.04 (0.02)} _{-0.04 (0.02)}	0.95±0.04
1442	11600889	12.521	5549±93	394±220	4.00 ^{+0.11 (0.10)} _{-0.12 (0.11)}	0.41±0.11
1445	11336883	12.320	6529±80	102±27	4.09 ^{+0.04 (0.01)} _{-0.04 (0.02)}	0.26±0.04
1474	12365184	13.005	6743±113	286±19	3.92 ^{+0.04 (0.02)} _{-0.04 (0.02)}	0.35±0.04
1478	12403119	12.450	5697±60	279±108	3.92 ^{+0.07 (0.05)} _{-0.07 (0.06)}	0.50±0.07
1525	7869917	12.082	6905±87	260±50	4.23 ^{+0.05 (0.03)} _{-0.05 (0.03)}	0.02±0.05
1529	9821454	14.307	6314±89	74±58	3.60 ^{+0.06 (0.04)} _{-0.06 (0.04)}	0.91±0.06
1530	11954842	13.029	6266±74	51±29	3.61 ^{+0.04 (0.01)} _{-0.04 (0.02)}	0.81±0.04
1531	11764462	13.069	6069±78	553±169	3.51 ^{+0.10 (0.10)} _{-0.04 (0.02)}	0.89±0.07
1532	11656246	12.841	6449±97	105±54	3.71 ^{+0.05 (0.03)} _{-0.05 (0.03)}	0.61±0.05
1534	4741126	13.470	6401±93	65±43	3.63 ^{+0.04 (0.02)} _{-0.05 (0.03)}	0.79±0.05
1535	11669125	13.046	6190±78	163±86	3.69 ^{+0.06 (0.04)} _{-0.06 (0.05)}	0.65±0.06
1536	12159249	12.710	6059±94	256±123	3.71 ^{+0.10 (0.09)} _{-0.08 (0.07)}	0.67±0.09
1573	5031857	14.373	6105±97	173±103	3.52 ^{+0.08 (0.07)} _{-0.05 (0.02)}	1.01±0.06
1667	5015913	12.989	5692±101	123±35	3.66 ^{+0.05 (0.03)} _{-0.05 (0.02)}	...
1740	6762829	13.941	5901±83	409±110	3.54 ^{+0.08 (0.07)} _{-0.06 (0.04)}	...
1814	5621125	12.538	7062±105	236±95	3.88 ^{+0.06 (0.05)} _{-0.06 (0.04)}	0.41±0.06
1822	5124667	12.443	6222±80	160±49	4.12 ^{+0.05 (0.02)} _{-0.05 (0.02)}	0.09±0.05
1886	9549648	12.239	6346±91	188±49	3.94 ^{+0.05 (0.02)} _{-0.05 (0.03)}	0.04±0.05
1909	10130039	12.776	6094±72	483±137	3.89 ^{+0.09 (0.08)} _{-0.09 (0.08)}	0.52±0.09
1952	7747425	14.601	6000±100	143±75	3.50 ^{+0.06 (0.05)} _{-0.04 (0.01)}	0.92±0.05
1964	7887791	10.687	5543±60	950±504	4.21 ^{+0.25 (0.24)} _{-0.25 (0.25)}	0.22±0.25
2008	8098728	10.800	6665±65	281±93	4.21 ^{+0.06 (0.04)} _{-0.08 (0.07)}	...
2025	4636578	13.781	6234±100	186±98	3.68 ^{+0.07 (0.05)} _{-0.07 (0.05)}	0.58±0.07
2027	8556077	11.826	6649±78	47±27	4.21 ^{+0.04 (0.02)} _{-0.04 (0.01)}	...
2075	10857519	12.217	6422±77	394±84	4.12 ^{+0.06 (0.05)} _{-0.06 (0.05)}	0.03±0.06
2086	6768394	13.959	6180±103	90±54	3.73 ^{+0.05 (0.03)} _{-0.05 (0.03)}	0.40±0.05
2087	6922710	11.863	6223±109	755±331	3.79 ^{+0.18 (0.17)} _{-0.17 (0.16)}	0.48±0.17
2110	11460462	12.189	6470±112	123±32	4.24 ^{+0.04 (0.02)} _{-0.04 (0.02)}	0.08±0.04
2148	6021193	13.353	5604±123	284±140	3.58 ^{+0.08 (0.07)} _{-0.09 (0.08)}	0.33±0.09
2149	10617017	12.071	6314±73	128±42	4.19 ^{+0.05 (0.02)} _{-0.04 (0.02)}	-0.02±0.05
2178	2014991	12.396	6420±101	299±121	3.83 ^{+0.09 (0.09)} _{-0.08 (0.07)}	...
2230	8914779	11.511	6266±84	163±55	4.14 ^{+0.05 (0.03)} _{-0.06 (0.04)}	...
2249	4761060	12.301	6756±107	259±61	3.92 ^{+0.06 (0.05)} _{-0.06 (0.04)}	...
2295	4049901	11.671	5453±93	46±32	4.19 ^{+0.04 (0.01)} _{-0.04 (0.01)}	0.29±0.04
2414	8611832	13.584	5889±74	54±32	3.87 ^{+0.04 (0.02)} _{-0.04 (0.02)}	0.64±0.04
2595	8883329	13.223	6741±115	95±42	3.88 ^{+0.05 (0.02)} _{-0.05 (0.02)}	0.23±0.05
2612	9602613	11.830	5450±59	56±24	4.31 ^{+0.04 (0.01)} _{-0.04 (0.01)}	...
5145	5263802	11.494	6916±105	428±95	4.14 ^{+0.06 (0.04)} _{-0.05 (0.04)}	...
5814	10616656	12.138	6506±85	233±202	4.19 ^{+0.10 (0.09)} _{-0.10 (0.09)}	...

^aThe top eight entries had no assigned KOI identifier at the time of writing.

^bEffective temperatures are from Pinsonneault et al. (2012).

^cUncertainties in brackets are produced by Eq. (2) and do not take into account the adopted figure of 0.04 dex for the accuracy.